Theses and Dissertations

1-1-2013

Effects of N-Type Doping on Algan Material Quality

Devendra Diwan
University of South Carolina

Follow this and additional works at: https://scholarcommons.sc.edu/etd

 Part of the Electrical and Electronics Commons

EFFECTS OF N-TYPE DOPING ON ALGAN MATERIAL QUALITY

by

Devendra Diwan

Bachelor of Science
University of South Carolina, 2010

_____

Submitted in Partial Fulfillment of the Requirements

For the Degree of Master of Science in

Electrical Engineering

College of Engineering and Computing

University of South Carolina

2013

Accepted by:

Goutam Koley, Director of Thesis

Grigory Simin, Committee Member

Lacy Ford, Vice Provost and Dean of Graduate Studies

ACKNOWLEDGEMENTS

ABSTRACT

The field of group III-nitride semiconductors has seen incredible developments during last couple of decades. They are recognized as the most promising materials for a wide field of optoelectronics and electronic devices. Their bandgap ranges from 6.2 eV for AlN to 0.7 eV for InN, covering a wide spectral range from infrared (1.77 mm) to deep ultraviolet (200 nm). Their direct bandgap makes them useful for fabricating optoelectronic devices such as light emitting diodes (LEDs), laser diodes (LDs), and photodetectors. III-nitride semiconductor materials also possess strong bond strengths and exhibit good structural, chemical and thermal stability. These properties make it possible for III-nitride based devices to operate in the high-temperature environments and also make them compatible with high processing temperatures. They also have high electron saturation velocity and high breakdown field. Such unique material properties also make III-nitride semiconductor very popular for the applications in high power, high frequency devices such as high electron mobility transistors (HEMTs).

AlGaN is the semiconductor materials of choice for optoelectronic devices in the ultra-violet (UV) spectral range and high power, high frequency electronic devices. Significant advances have been made in AlGaN based UV light emitting diodes high electron mobility transistors during the last decade. Performance and reliability of these devices strongly depend on the electronic properties of epitaxial layers which are critically affected by structural defects and unintentional doped impurities. As the bandgap of AlGaN increases with its Al composition, the ionization energies for silicon

(n-type dopant) and magnesium (p-type dopant) increase too, resulting in a lower ionization efficiency. Therefore, both n-type and p-type doping of AlGaN layers is much more difficult than GaN. Very high Si doping concentration is needed to achieve low resistivity AlGaN layers.

Effective doping without compromising material quality is the key to high efficiency of AlGaN based devices. This thesis is focused on optimization of AlGaN epitaxial growth and the effects of n-type doping on AlGaN epilayer quality. AlGaN films were grown on c-plane sapphire substrates using metal organic chemical vapor deposition. First growth optimization of AlGaN layer was carried out. A systematic study of a series of Si-doped $Al_xGa_{1-x}N$ layers with three different x = 50%, 65% and 72% was accomplished. Detailed material characterization including x-ray diffractometry, atomic force microscopy, hall-effect measurement, sheet resistance mapping, and transmission line measurement was carried out. As the doping concentration increased, carrier concentration was found to monotonically increase whereas doping efficiency reduced. Hall mobility and carrier concentrations were found to reduce with increased Al concentration, as expected due to increased ionization energy. Calculated doping efficiency was found to be consistent with doping efficiency equation. The comprehensive results, relevant conclusions and future trends are included.

TABLE OF CONTENTS

LIST OF TABLES

LIST OF FIGURES

CHAPTER 1: INTRODUCTION

Chapter 1 reviews the history and scientific breakthroughs in the field of III-nitrides. Nitride-based device structures for electronic and optoelectronic applications usually incorporate layers of $Al_xGa_{1-x}N$, where $0 \leq x \leq 1$ depending on the targeted wavelength or specific application. The layers could be binary, ternary or quaternary type of semiconductors and may be undoped or doped with p- or n- type of impurities. Various growth techniques, their current status and challenges associated with heteroepitaxy of AlGaN films are also discussed in this chapter.

The field of group III-nitrides has seen remarkable developments during last two decades. They are recognized as the most promising materials for a wide field of optoelectronics and electronic devices.
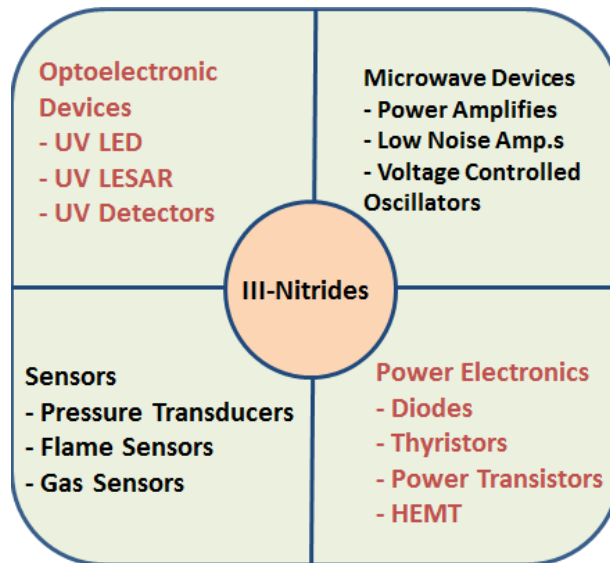
Figure 1.1: Applications of III-Nitride Semiconductors

They are wide bandgap materials and crystallize in wurtzite or zinc blende polytypes, the wurtzite being the most common. Their bandgap ranges from 6.2 eV for AlN to 0.7 eV for InN, covering a wide spectral range from infrared (1.77 mm) to deep ultraviolet (200 nm) [1]. Their direct bandgap makes them useful for fabricating optoelectronic devices such as Light Emitting Diodes (LEDs), laser diodes, and photodetectors. III-nitride semiconductor materials also possess strong bond strengths and exhibit good structural, chemical and thermal stability. These properties make it possible for III-nitride based devices to operate in the high-temperature environments and also make them compatible with high processing temperatures. They also have high electron saturation velocity ($2x10^7$ cm/s) and high breakdown field (~2 MV/cm). Such unique material properties also make this III-nitride semiconductor very popular for the applications in high power, high frequency devices such as High Electron Mobility Transistors (HEMTs).

1.1   EVOLUTION OF III-NITRIDE FILMS AND CRYSTALS GROWTH

As reviewed by Ambacher the history of group III-nitrides covers more than a century. AlN powder was first made in 1862 from liquid Al and N_2 gas. The major drawback of this direct reaction method is that the surface film of AlN on Al is highly adherent and hinders further reaction. Almost a century later in 1964 a more useful method for making AlN is to react AlF_3 powder with NH_3 gas at high temperatures. The overall chemical reaction at 1000 ^{o}C is:

$$AlF_3(s) + NH_3\,(g) \rightarrow AlN(s) + 3HF\,(g) \quad \dots\dots\dots\dots\dots 1.1$$
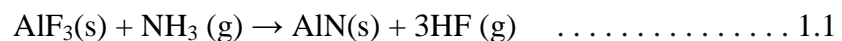
In order to promote the formation of AlN, it is necessary to keep the NH3 partial pressure above 1 bar and the HF gas must be continually removed. At 1 atm. pressure, a

minimum of 25 molecules of NH3 are needed for each AlN molecule produced. The earliest investigations of GaN powder were reported by Johnson and co-workers, who described the conversion of metallic Ga in a NH3 stream by the chemical reaction:

$$2Ga \text{ (l)} + 2NH_3 \text{ (g)} \rightarrow 2GaN(s) + 3H_2 \text{ (g)} \quad \dots \dots \dots \dots \dots 1.2$$
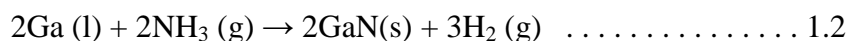
They obtained a black powder by flowing ammonia over metallic gallium at $1000^{o}C$. These early growth processes and investigations resulted in AlN and GaN powders and very small crystals which were used to determine basic physical properties like crystal structure, lattice constants and optical properties. These results enabled the identification of substrate materials suitable for the heteroepitaxy of group III-nitrides [2].

The first demonstration of growth of GaN and AlN films by MOCVD was carried out by Manasevit *et al*. in 1971. However, the first p-n junction GaN-based LED by MOCVD was achieved much later in 1989 by Amano and Akasaki *et al*. [2] [3] . Akasaki and his collaborators showed that good epilayers of III–nitrides on sapphire substrates can be grown by MOCVD if the growth is performed in two steps. Various epitaxial growth techniques and its uniqueness are briefly discussed here.

1.2 CURRENT EPITAXIAL GROWTH TECHNIQUES

Molecular beam epitaxy (MBE), hydride vapor phase epitaxy (HVPE), and metal organic chemical vapor deposition (MOCVD) are the three common methods used for growth of III-nitride epilayers.

1.2.1 Molecular beam epitaxy

MBE can produce high-quality layers with very abrupt interfaces and good control of thickness, doping, and composition. MBE growth mechanism is shown in

Figure 1.2 [3]. It involves evaporation of the source materials and layer-by-layer growth on a hot substrate.
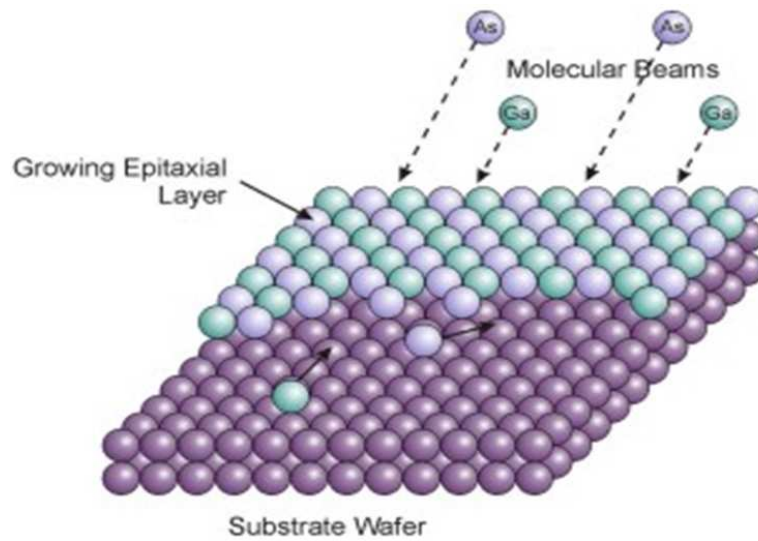
Figure 1.2: MBE growth mechanisms

Typically atoms are delivered as a beam of gas onto the substrate under extremely high vacuum. Atoms arriving at the substrate surface may undergo absorption to the surface, surface migration, incorporation into crystal lattice and thermal desorption. Which of the competing pathways dominates the growth will strongly depend on the temperature of the substrate. Growth temperatures are usually much lower than for MOCVD to avoid evaporation of the group III material. Since N2 cannot be dissociated by using conventional effusion cells, alternate nitrogen sources are usually employed. Use of ammonia as a nitrogen source results in very low growth rates as ammonia is very stable at lower temperatures. Plasma sources can be used to grow high quality GaN at growth rates comparable to MOCVD. However, due to the need for ultra-high vacuum in MBE, MOCVD still remains the most favored growth method of III-Nitrides [1].

1.2.2 Hydride vapor phase epitaxy

HVPE technology was used to deposit epilayers of both GaN and AlN more than 40 years ago. The method provides deposition rates of several microns per minute making it possible to grow hundred microns thick layers. H.P. Maruska et al. [1] used HVPE to demonstrate the first GaN violet light emitter. AlGaN alloy growth by HVPE has also been performed. However, despite substantial progress in material quality and process understanding, background n-type carrier concentration in grown materials remained high and achieving p-type conductivity was very challenging. Rapid progress in MOCVD for p-type GaN and AlGaN materials in the early 1990s and its ability to form a (Al)N/InGaN quantum well structures made HVPE technology obsolete for growth of device structures.

1.2.3 Metal organic chemical vapor deposition
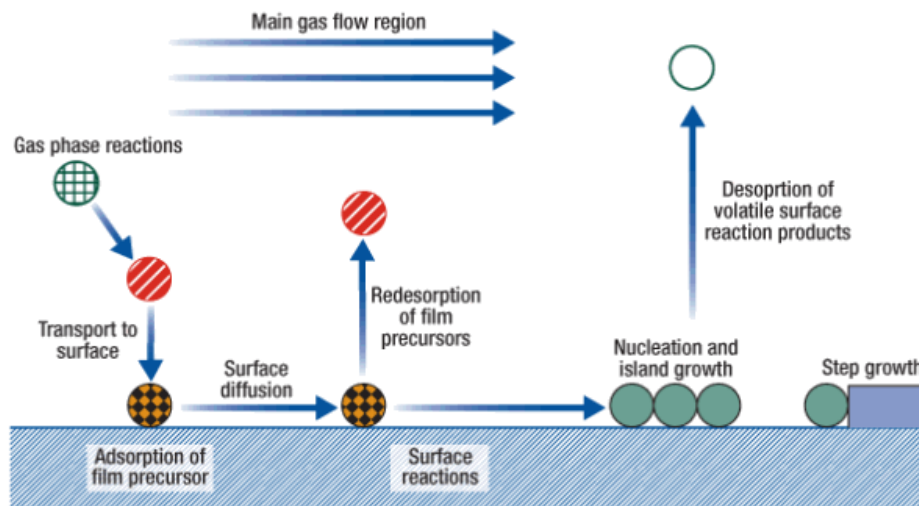
Figure 1.3: MOCVD process [4]

MOCVD has developed over the past two decades into the leading technique for epitaxial growth of group III-nitrides. This technique was first introduced in the late

5

1960s by Manasevit and Simpson to deposit GaAs films onto foreign substrates. The near equilibrium technique such as HVPE is not suitable for nucleation onto a chemically different surface. These pioneers found that if they used combination of an alkyl organometallic for the group III element and a hydride for group V element, then films of GaAs could be deposited on a variety of different surfaces. Thus the technique of MOCVD was born and in the late 1980s it became the main production technique after improving the purity of organometallic precursors and hydrides.

As shown in Figure 1.3, growth by MOCVD involves gas phase transport of organometallic precursors, hydrides and carrier gases to a heated substrate. Higher growth temperatures allow the volatile precursors to pyrolize at the substrate and deposit a nonvolatile solid film. The group III sources are usually Trimethylgallium (TMGa), Trimethylaluminum (TMAl) and Trimethylindium (TMIn) whereas high-purity ammonia (NH_3) is used as the hydride source. Silicon (Si) is the most common n-type dopant and is delivered in hydride forms, such as silane (SiH_4) and disilane (Si_2H_6) whereas Mg is the most common p-type dopant.

1.3   SUBSTRATE SELECTION AND ISSUES

Unlike other semiconductors, growth of native III-nitride substrates is extremely challenging. The key obstacle is the low solubility of N_2 in metal melts at reasonable temperatures and pressures coupled with high vapor pressure of N_2 above nitrides [2]. Therefore the standard methods of crystal growth used for producing semiconductor substrates (such as Bridgman, Czochralski, Verneuil) cannot be used for III-nitrides. Bulk GaN and AlN substrates are now commercially becoming available. Growing epi-layers on native substrate are beneficial due to no lattice mismatch. Growth on native substrate

can produce epi-structure with a very low dislocation density but these substrates are very expensive and available in smaller sizes of about 1 inch diameter. Due to their high cost and limited size bulk substrates are not preferable for industrial applications. The bulk AlN substrate also has a high light absorption rate which makes them inefficient for optoelectronic applications. The substrate selection becomes crucial in the field of III-nitride due to all constrains associated with native substrates. The growth over foreign substrate has been mature over this period. A wide variety of foreign substrate materials have been studied by various groups for nitride epitaxy, including sapphire, SiC, Si, GaP, W, ZnO, $MgAl_2O_4$, MgO, $LiAlO_2$, and $LiGaO_2$. The most promising results so far have been obtained on sapphire, Si, and SiC. However, there is significant mismatch of lattice constants as well as thermal expansion coefficients (TEC) between III–nitrides and these substrates as shown in following Table 1.1 [1] [2]

Table 1.1: Mismatch of lattice constants and thermal expansion coefficients between III-nitride and most favored foreign substrates.

Substrate/III-Nitrides	Lattice mismatch (%)			TEC mismatch (%)		
	AlN	GaN	InN	AlN	GaN	InN
Sapphire	11.73	13.86	22.58	-44.67	-25.47	-24
Si (111)	-23.38	-20.91	-9.37	59.62	115	119
SiC – 6H	1.03	3.42	14.68	-1.19	33.1	35.71
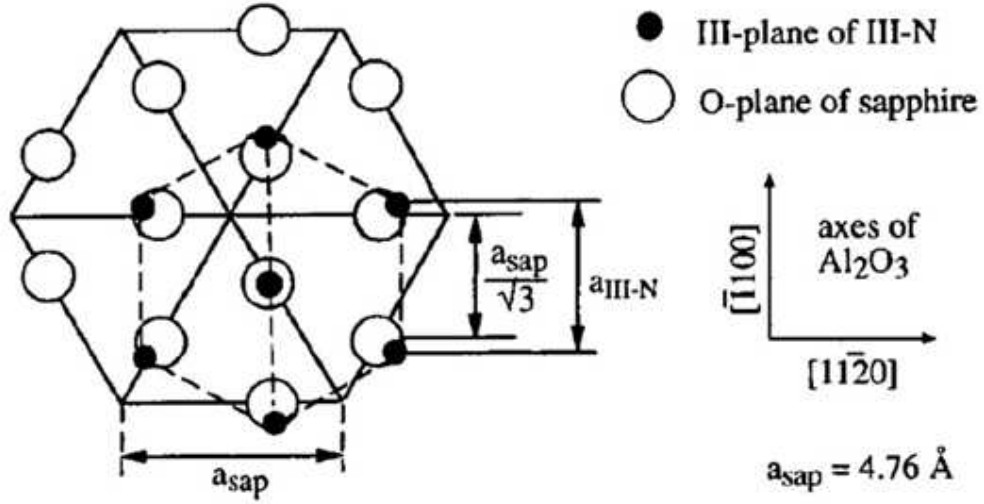
Figure 1.4: Schematic representation of in-plane atomic arrangement in the case of (0001) AlN film grown on (0001) sapphire [2]

In spite of large differences in lattice parameters and TECs, heteroepitaxy of nitrides on c-plane sapphire has produced the best device performance to date. As shown in Table 1.1 the lattice mismatch of GaN with sapphire is ~14 %. The quality of the films grown directly on sapphire without buffer layer is poor and hillocks are observed because of the large mismatch of lattice and thermal expansion of GaN and sapphire. The schematic representation of in plane atomic arrangement in the case of AlN film grown on sapphire is shown in Figure 1.4. Later in this thesis growth of better quality epitaxial layer by first growing low temperature nucleation layer, its experiments and results are discussed. Large-area high-quality sapphire substrates are easily available at low cost. These substrates are also available in wide range of diameter and thickness. They are transparent, stable at high temperature, and the growth technology of nitrides on them is rather established.

1.4   III-Nitrides thin films for Optoelectronic Applications
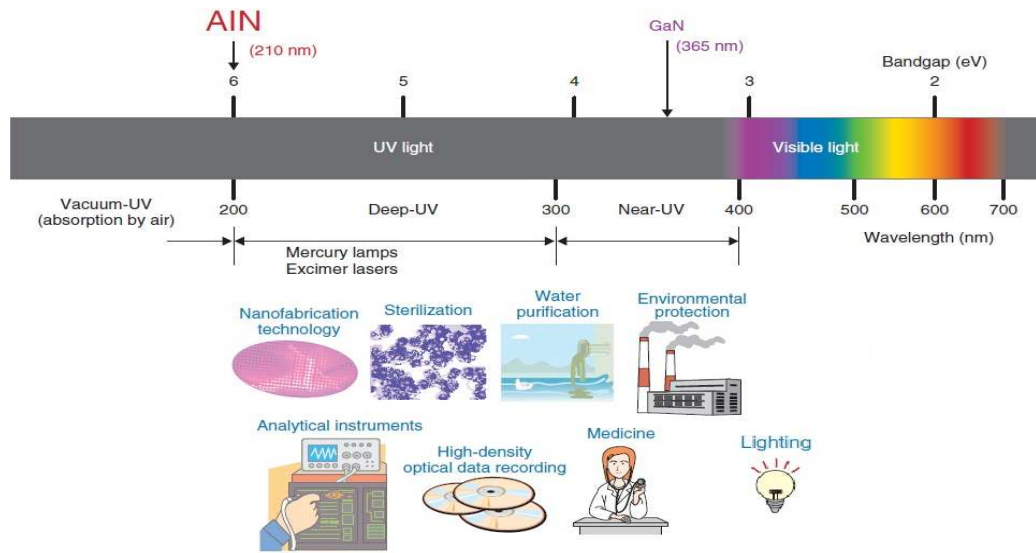
Figure 1.5: UV LED Applications [5]

GaN-based semiconductors as wide-band gap materials have found increasing scientific and practical interest in the recent years. This is in large part, due to their use in high power light-emitting diodes (LEDs) as well as laser diodes (LDs) in addition to their application for high power high frequency electronics [2]. The LEDs emit infrared rays, visible light, or ultraviolet (UV) rays. The visible range of LEDs plays an important role in high density optical storage, solid-state lighting, color printing and display applications.

As shown in the ultraviolet LEDs (UVLEDs) have potential use in disinfection, sensing and polymer curing. Emission light in deep-UV band with short wavelengths of between 220 and 350 nanometers has high sterilizing power. UVLEDs overall have a growing potential in a broad range of applications, including in medicine and in the rapid decomposition of environmental pollutants, such as dioxins.

9
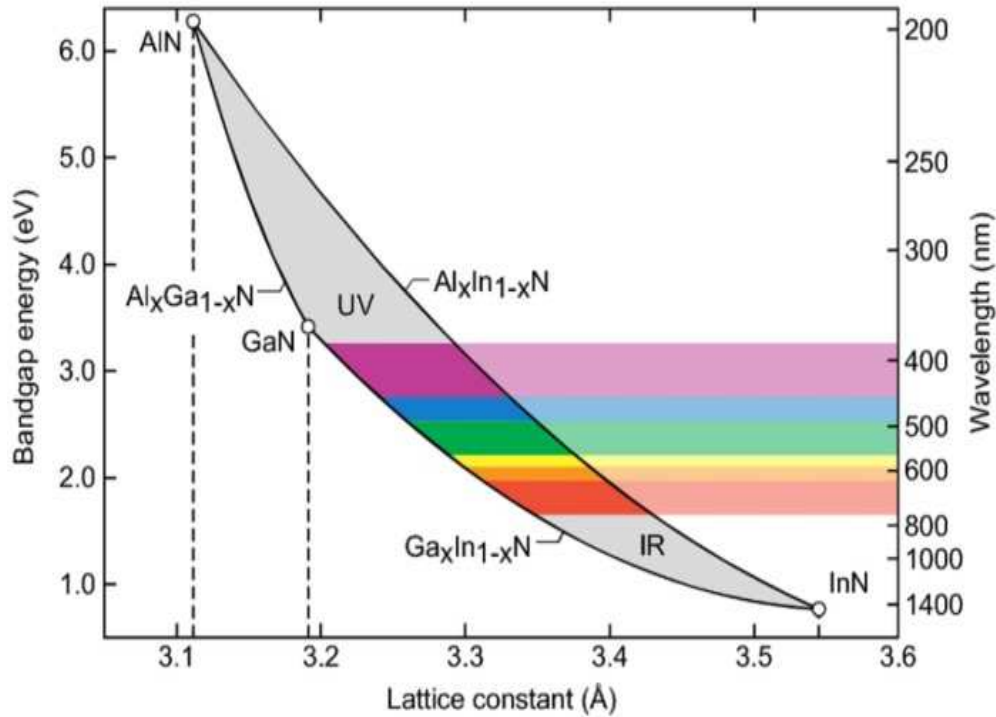
Figure 1.6: Bandgap and wavelength as a function of lattice constant for AlGaInN [1]

AlN, GaN and InN are all direct bandgap semiconductor; the bandgap energy for AlN is 6.2 eV, for GaN it is 3.4 eV and for InN it is 0.6. Figure 1.6 shows the bandgap energy and wavelength as a function of lattice constant. Unlike the III-phosphide semiconductor materials the III-nitride system enables LEDs that emit green, blue, violet and even ultraviolet wavelengths.

The LEDs typically consists of n-type and p-type layers made from GaN or AlGaN, quantum wells made from GaInN or AlGaN and blocking layers made from AlGaN. In a semiconductor with a bandgap Eg, recombination of an electron-hole pair (EHP) leads to the release of an amount of energy equal to Eg. One way this energy can be released is through an emission of a photon. The wavelength λ of this emitted photon is governed by the bandgap of the semiconductor material according to the following equation:

$$\lambda = \frac{h\,c}{E_g} \qquad\qquad \cdots\cdots\cdots\cdots 1.3$$

Thus, a light source of a desired wavelength can be engineered by using a semiconductor with a proper bandgap and the bandgap is controlled just by changing the group-III content [1]. Blue LEDs are particularly attractive for solid-state lighting applications; for the application the blue LEDs are combined with yellow phosphors to make white light source.

1.4.1 Light Emitting Diodes

The schematic of typical LED is shown in Figure 1.7.
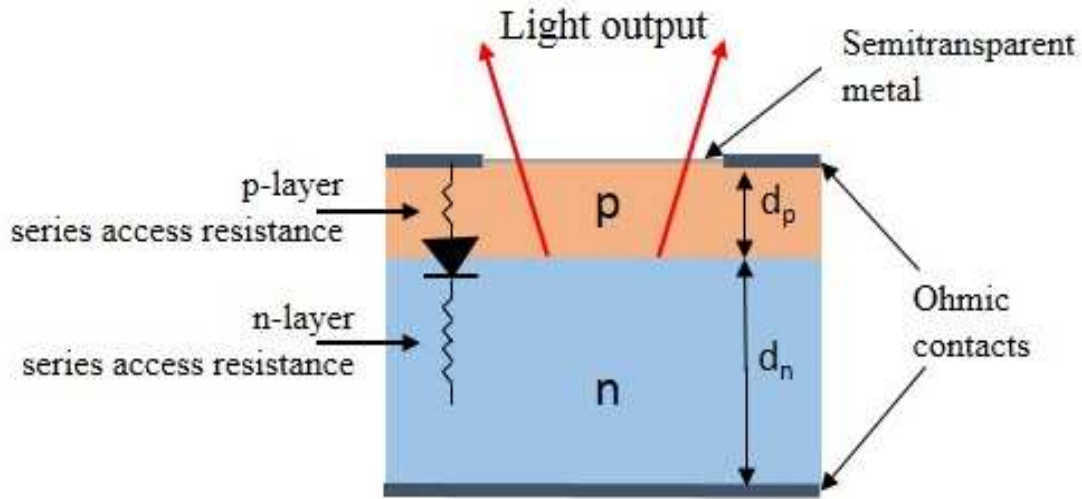
Figure 1.7: Schematic of typical LED

The whole structure is grown by epitaxial technique using MOCVD process. The device is usually designed such that most of the radiative recombination takes place in the side of the junction nearest the surface whereby the probability of reabsorption is greatly

11

reduced. The process occurring in a LED can be divided into three stages and the overall device efficiency η_o, may be expressed as per following equation:

$$\eta_{o} = \eta_{in}\, \eta_{r}\, \eta_{e} \qquad \ldots\ldots\ldots\ldots\ldots 1.4$$

where, η_{in}, η_{r}, and η_{e} respectively are the injection, radiative recombination, and extraction efficiency.

The overall LED efficiency is simply the ratio of optical power output and electrical power input. Thus, efficiency depends on electrical efficiency and light extraction efficiency.

Wall-plug power efficiency may be expressed as shown in following equation:

$$\eta_{wp} = \frac{P_{optical}}{P_{electrical}} \qquad \ldots\ldots\ldots\ldots\ldots 1.5$$

This efficiency can be significantly improved by minimizing $P_{electrical}$, which is controlled by n-layer and p-layer series access resistance, denoted respectively, R_{sn} and R_{sp}.

$$R_{sn} = \rho_n\, \frac{d_n}{A} \qquad \ldots\ldots\ldots\ldots\ldots 1.6$$

where, the resistivity of the n-layer is ρ_n, the thickness is dn and contact area is A.

$$R_{sp} = \rho_p\, \frac{d_p}{A} \qquad \ldots\ldots\ldots\ldots\ldots 1.7$$

where, the resistivity of the p-layer is ρ_n, the thickness is dp and contact area is A [3].

The resistivity of both n- and p- type of layers can be improved by effective doping of these layers. Hence, doping plays a crucial role in improving efficiency of light emitting diodes (LEDs).

1.4.2 Visible Light Emitting Diodes

The past decade has seen an explosion in the usage of solid-state lighting, vastly enhancing the quality of our life.

Figure 1.8: A dress consisting of 2000 LED lights displays live tweets during Britain's 4G mobile network launch

The single color LEDs has been commercialized with significant improvement in its lifetime. The simplified structure of typical InGaN based LED is shown in the Figure 1.9.
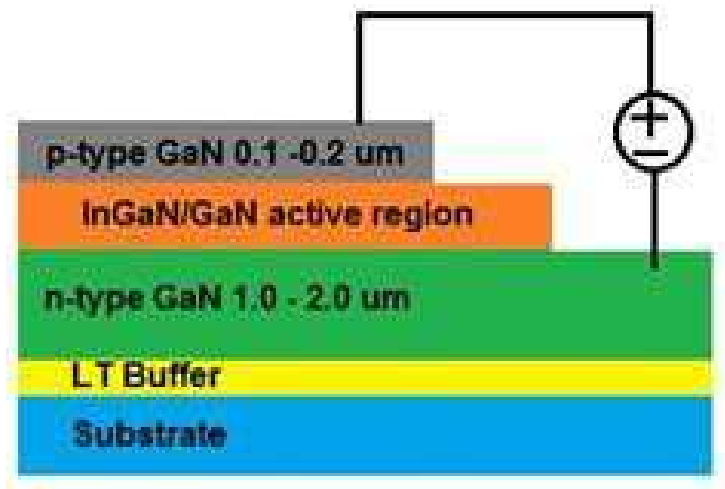
Figure 1.9: Simplified structure of a typical InGaN based LED

Currently, wide verity of LEDs and Laser Diodes are used for various applications. Figure 1.8 shows one of the advanced applications of visible LED being used as a unique display platform. The real revolution in lighting technology will occur if we are able to replace our conventional white light source with LEDs.

The most straightforward way to generate white light is to simply combine monochromatic light of the three primary colors: red, green, and blue (RGB). This will produce a white source matching the RGB sensors of the human eye [6]. However, the growth of InGaN with higher In content is intrinsically difficult. The dissociation temperature of InN (~600° C) is lower than the general growth temperature range for nitrides (~1000° C) and thus the growth temperature of InGaN should be lower. On the other hand, the decomposition efficiency of NH3 decreases drastically around 600° C. Because of the difficulties faced with the growth of red- emitting InGaN, Philip *at el* considered other potential white light sources; particularly ones in which only require emission wavelengths <600 nm.

This approach of combining different colors to produce white light is shown in Figure 1.10. One such example is the two-color structure shown in Figure 1.11. This device structure features two independently-powered active regions which emit at approximately 400 nm and 560 nm. These two wavelengths are known to be complementary and they can be mixed to yield an overall emission which gives the perception of white light.
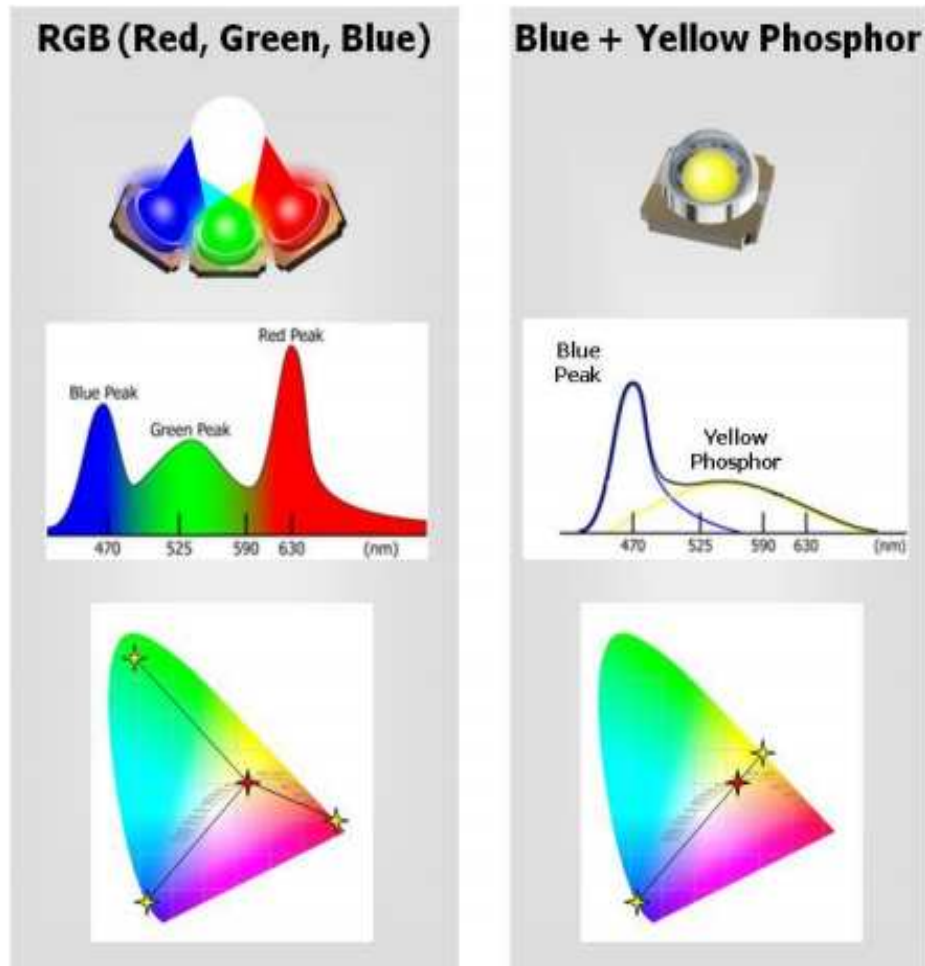
Figure 1.10: Two ways to produce white lite with LEDs [10]
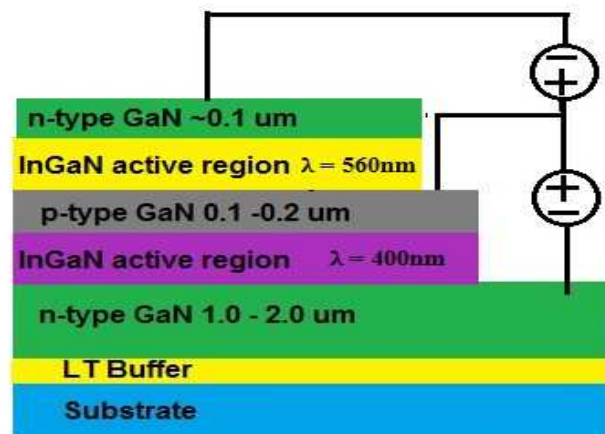
Figure 1.11: White LED structure using violet and yellow emission
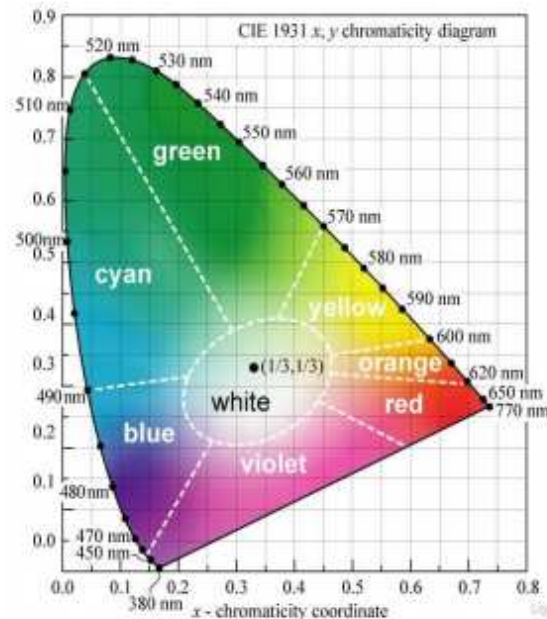
Figure 1.12: Enhanced version of the CIE Chromaticity Diagram

This is often demonstrated by the enhanced version of the 1931 CIE chromaticity diagram shown in Figure 1.12 [7]. Pure or saturated colors are located around the perimeter of the parabolic and white light is located at its center. A key aspect of colorimetry is that color perception is essentially an additive function of the color space. Human color perception can be such two light source made up of different wavelengths may appear to be the same color.

Thus two light sources will have the same apparent color to an observer when they have the same tristimulus values, no matter what spectral distribution of light were used to produce them. Two sources that have the same trichromatic values will also have the same resulting chromaticity point in the color space.

1.4.3 Ultra Violet Light Emitting Diodes (UVLEDs)
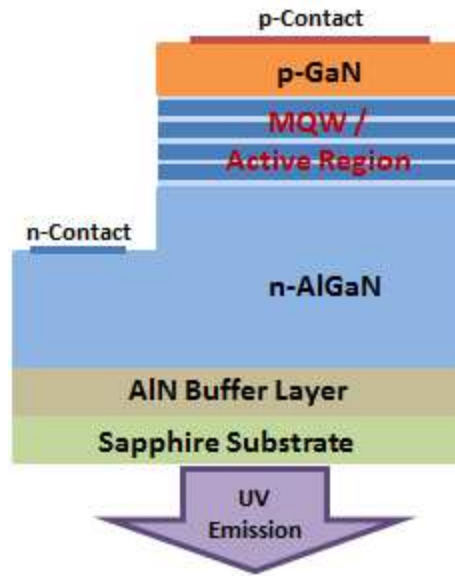
Figure 1.13: Schematic of UVLED on sapphire

The UVLED layer structure is shown in Figure 1.13 [8]. The growth of epitaxial structure is done over basal plane sapphire substrate by MOCVD process. The UVLED typically consists of MQW active region sandwiched between n-AlGaN and p-GaN layers. Both the Al compositions of AlGaN barrier layers, n-AlGaN and p-AlGaN cladding layers are also adjusted to preserve the carrier confinement in quantum wells and proper injection conditions and the optical transparency of cladding layers. Superlattices between AlN and n-AlGaN layer minimizes cracking by modifying strain properties of the epilayer structure and thus significantly improves the electrical properties of n-AlGaN. There are still several issues in achieving more reliable UVLEDs with higher efficiency, which is ~ 10 % as compared to the efficiencies of visible LEDs ~ 70%. Novel ways of improving and optimizing layer structure of UVLED would possibly boost its performance and efficiency.

1.5   SCOPE OF STUDY

As discussed earlier in this chapter, AlGaN is the semiconductor materials of choice for optoelectronic devices in the UV spectral range and high power, high frequency electronic devices. Significant advances have been made in AlGaN based UV light emitting diodes high electron mobility transistors during the last decade. Performance and reliability of these devices strongly depend on the electronic properties of epitaxial layers which are critically affected by structural defects and unintentional doped impurities. As the bandgap of AlGaN increases with its Al composition, the ionization energies for silicon (n-type dopant) and magnesium (p-type dopant) increase too, resulting in a lower ionization efficiency. Therefore, both n-type and p-type doping of AlGaN layers is much more difficult than GaN. Very high Si doping concentration is needed to achieve low resistivity AlGaN layers.

Effective doping without compromising material quality is the key to high efficiency of AlGaN based devices. This thesis is focused on optimization of AlGaN epitaxial growth and the effects of n-type doping on AlGaN epilayer quality. First, growth optimization of AlGaN layer was carried out. In Chapter 2, optimization of AlGaN layer and importance of nucleation layer is discussed. AlGaN films were grown on c-plane sapphire substrates using metal organic chemical vapor deposition. Chapter 3 covers a systematic study of a series of Si-doped $Al_xGa_{1-x}N$ layers with three different x = 50%, 65% and 72%. This chapter also includes material characterization including x-ray diffractometry, atomic force microscopy, hall-effect measurement, sheet resistance mapping, and transmission line measurement. Effects of doping on $Al_xGa_{1-x}N$ with change in x value and doping concentration are examined. The comprehensive results

from these characterizations including carrier concentration and doping efficiencies are reported. Relevant conclusions and future trends are discussed in Chapter 4 and 5.

CHAPTER 2: OPTIMIZATION OF ALGAN EPITAXIAL GROWTH

To fabricate nitride-based ultraviolet optoelectronic devices, a deposition process for high-Al-composition AlGaN (Al content > 50%) films with reduced dislocation densities must be developed. This chapter describes the growth of AlN and AlGaN film on (0001) sapphire via a LT AlN nucleation layer using metal organic chemical vapor deposition (MOCVD). The influence of the low temperature AlN buffer layer thickness on the AlN epilayer is investigated by triple-axis X-ray diffraction, optical microscope and optical transmission. The results from sample characterization have been discussed later in this chapter. An appropriate buffer thickness results in the best structural properties and surface morphology [9] [10].

2.1 TWO STEP EPITAXIAL GROWTH PROCESS

Until 1985, hexagonal GaN grown by MOCVD was deposited directly on sapphire substrates. The fabricated epitaxial GaN films had rough surfaces mainly caused by the three-dimensional growth mode, which resulted in the surface morphology shown in the Figure 2.1. In 1986, Amano et al succeeded in remarkably improving the surface morphology as well as the electrical and optical properties, by deposition of a 50 nm thick AlN film on c- plane sapphire as a nucleation layer, before GaN film growth by MOCVD [11].

20
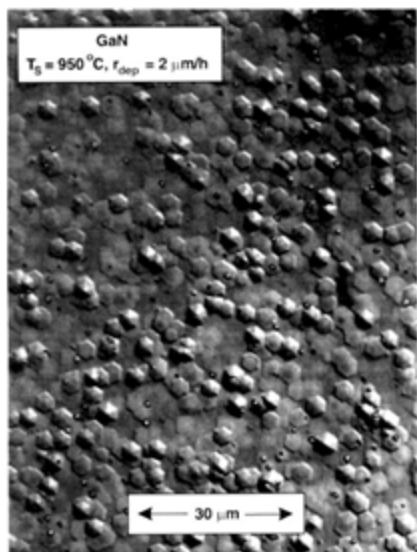
Figure 2.1: Surface micrograph of GaN

The growth process is shown schematically in Figure 2.2. The essential role of a low-temperature buffer layer is both to supply nucleation centers having the same orientation as the substrate and to promote lateral growth of the GaN film due to the decrease in interfacial free energy between the film and the substrate. Prior to the first step, the sapphire substrate is heated to high temperature $(1000 - 1100\ ^{o}C)$ in hydrogen environment. The substrate may also be annealed in NH_3 gas to nitridate the growth surface. The temperature is then reduced $(600 - 700\ ^{o}C)$ for the first step growth and a low temperature AlN or GaN nucleation layer (LT-NL) with a thickness in the range of $200 - 500\ A^{o}$ is deposited. The microstructure of LT-AlN is composed of fine crystallites with diameters of $30 - 50\ A^{o}$. After the growth of nucleation layer, the substrate is heated to the normal growth temperature of $\sim 1000\ ^{o}C$ for GaN growth. During the heat up, LT-AlN layer rearranges from fine crystallites into columns with diameters of $100 - 500$ nm. In the second growth step, GaN islands nucleate on LT-AlN and then grow laterally. The threading dislocations are generated as a result of coalescence of adjacent islands.

21
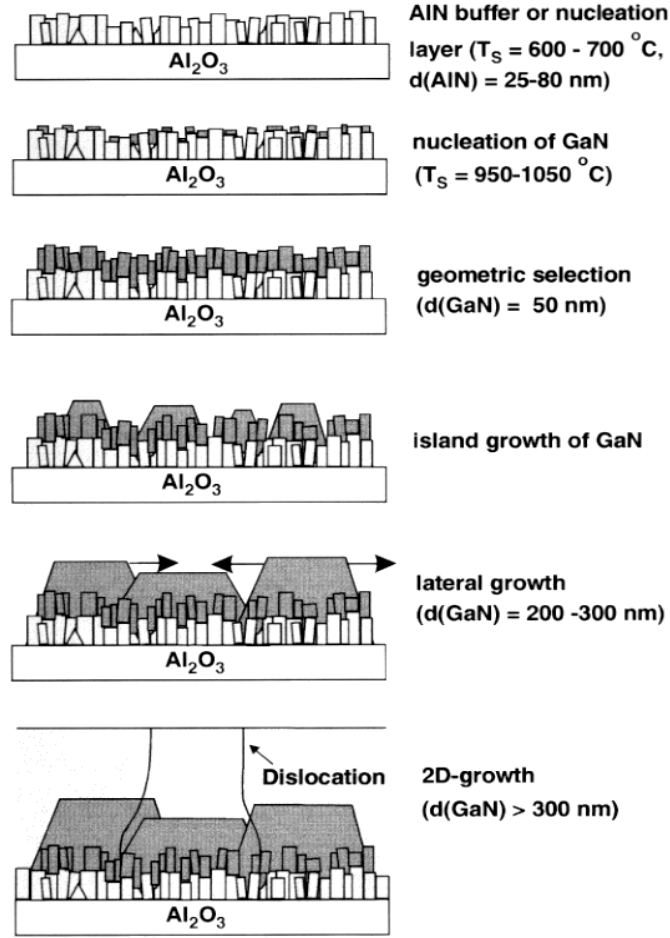
Figure 2.2: Schematic diagram of the growth process proposed by Amano *et al*

2.2 NUCLEATION LAYER

Samples for optimization of nucleation layer are grown on c-plane sapphire substrate via a low temperature nucleation layer by MOCVD. Hydrogen is employed as a carrier gas. A growth pressure of 50 Torr is used along with 1100°C growth temperature. Microscopic images, AFM scans and X-ray rocking curves techniques have been used to characterize these samples. For this thesis four AlN samples A, B, C and D are grown and results have been discussed. Keeping growth conditions constant only buffer thickness have been varied by changing buffer growth time as shown in Table 2.1.

Table 2.1: Sample details for buffer optimization

AlN Samples	Sample A	Sample B	Sample C	Sample D
Buffer thickness [Å]	200	245	253	271
X-ray, Omega scan FWHM [arcsec]	30.2	9.1	12.7	14.4
Surface roughness Root mean square [Å]	54	1.27	0.9	1.09

2.3   RESULTS AND DISCUSSION

The results show that the buffer thickness is a key parameter that affects the quality of the AlN epilayer. As shown in Figure 2.3, optical spectrum of Sample A shows poor optical properties from the slope. However, Sample B shows no optical degradation.
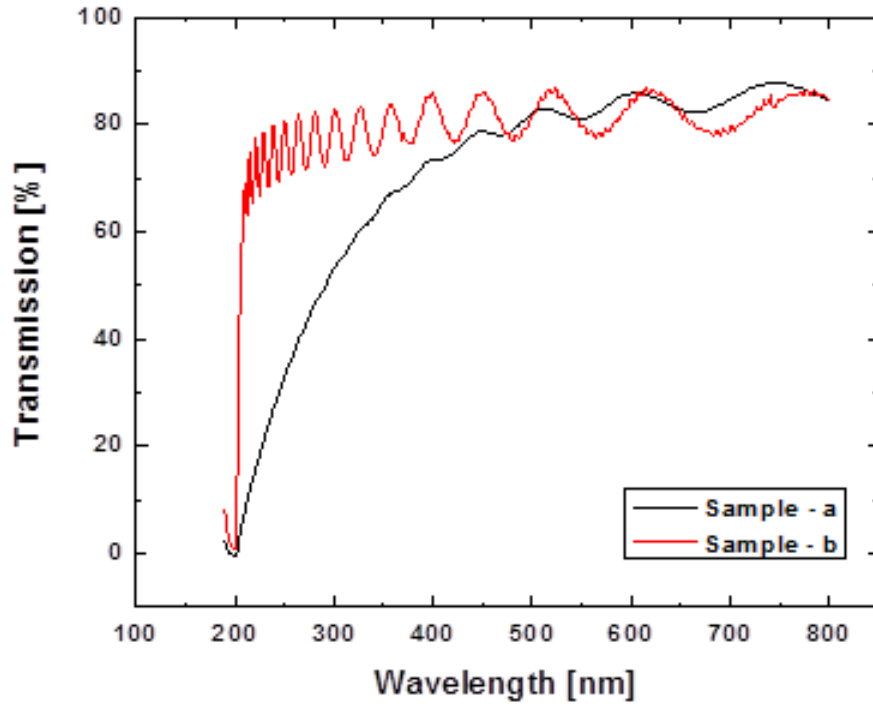
Figure 2.3: Optical transmission for sample A and B
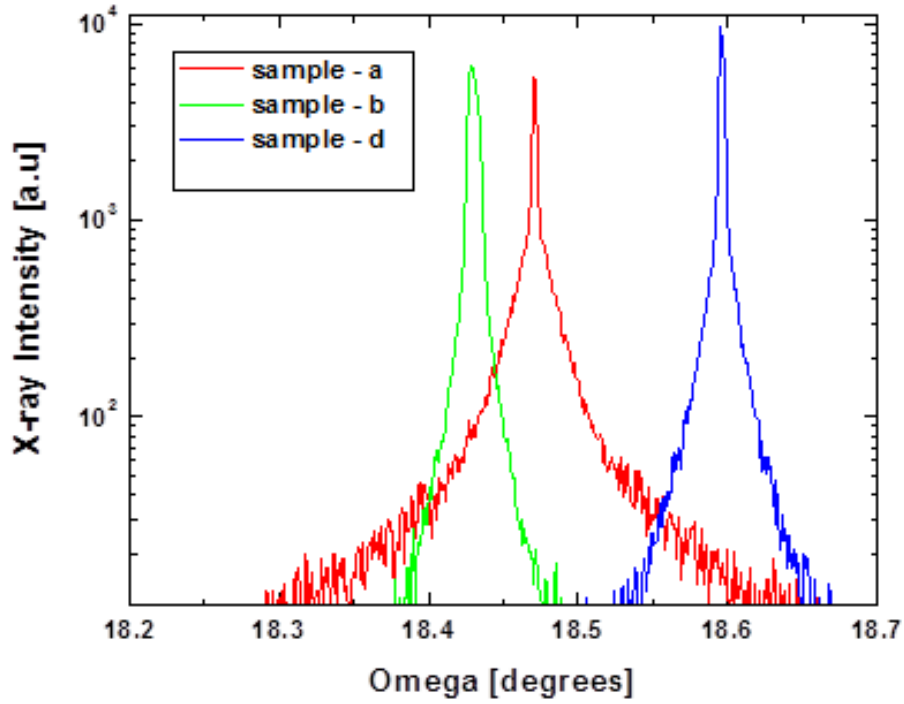
Figure 2.4: X-ray omega scan

Full width half maximum (FWHM) of the x-ray diffraction scan shows the crystal quality. From Table 2.1 it is clear that sample A FWHM is almost double than sample B, C, and D. Surface roughness scan of Atomic Force Microscopy (AFM) shows very rough surface of sample A, 54 angstrom. We can clearly see much lower RMS roughness for optimized samples B and C.

Sample D with buffer thickness has equally good RMS roughness of its surface, but microscopic images shows heavy edge cracking. This is the effect of higher than optimized buffer layer thickness.

(a)

(b)

(c)
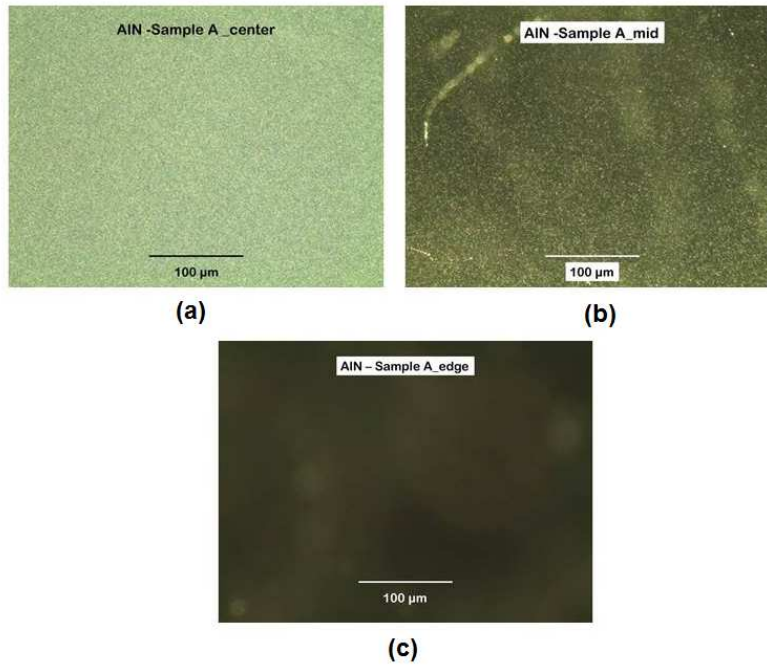
Figure 2.5: Microscope Images of *Sample - A* AlN thin film with 200 angstrom thick nucleation layer

(d)

(e)
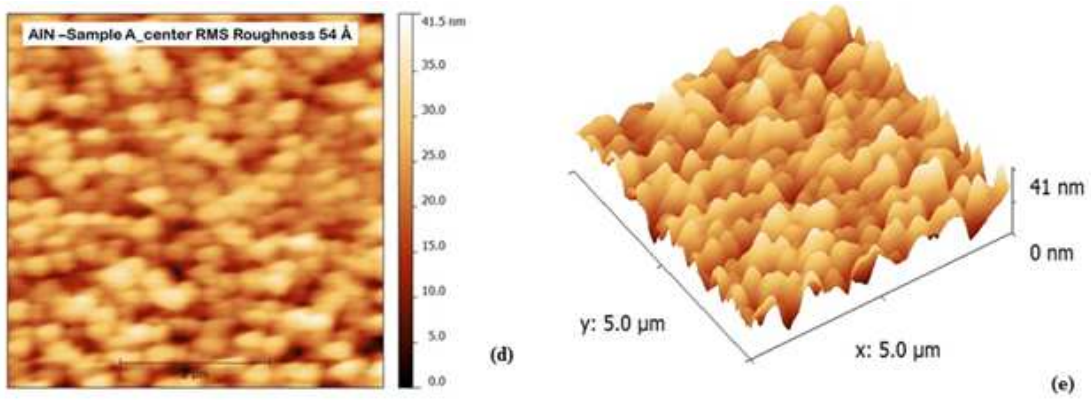
Figure 2.6 AFM scan of AlN thin film with thinner nucleation layer
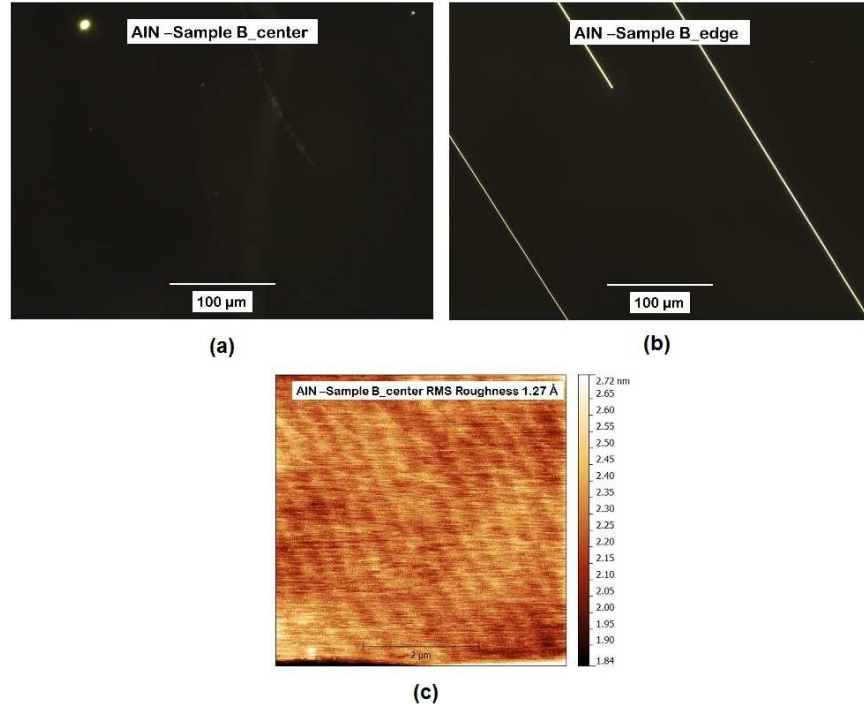
Figure 2.7: Microscope Images (a) and (b) and AFM scan (c) of AlN thin film with optimized nucleation layer of 245 angstrom.
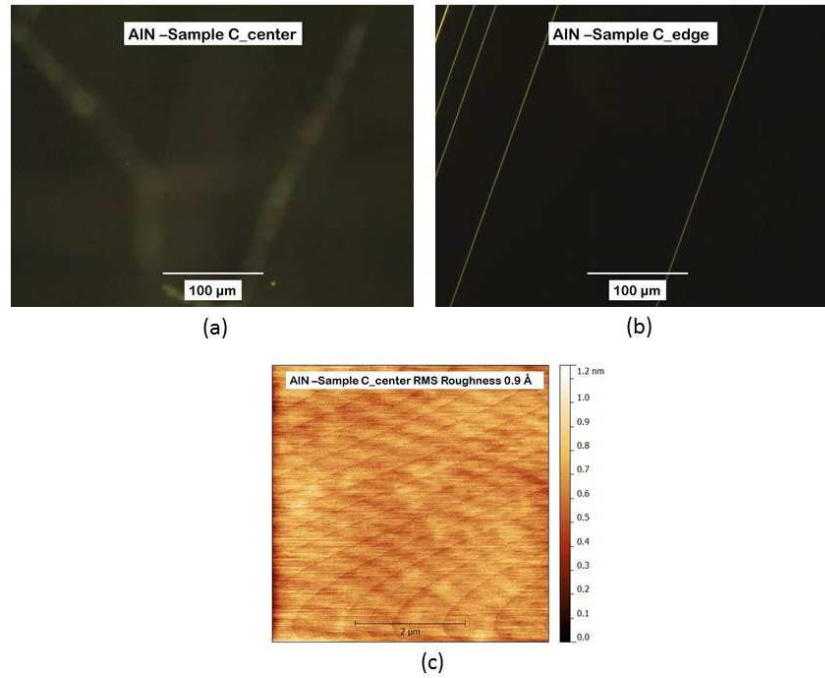
Figure 2.8: Microscope Images (a) and (b) and AFM scan (c) of AlN thin film with optimized nucleation layer of 253 angstrom.
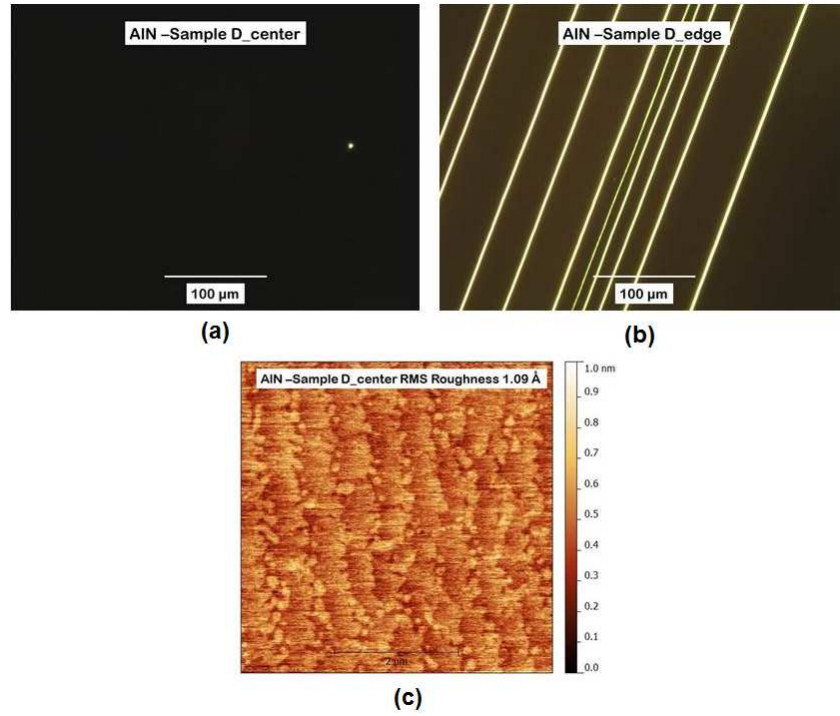
Figure 2.9: Microscope Images (a) and (b) and AFM scan (c) of AlN thin film with 271 angstrom thick nucleation layer

CHAPTER 3: EFFECTS OF N-TYPE DOPING ON ALGAN MATERIAL QUALITY

When electron–hole pairs are generated in a semiconductor, or when carriers are excited in to higher impurity levels from which they fall to their equilibrium states, light can be given off by the material. Compound semiconductor with direct band gaps are more suitable for light emission. The general property of light emission is called luminescence. This overall category can be subdivided according to the excitation mechanism: If carriers are excited by photon absorption, the radiation resulting from the recombination of the excited carriers is called photoluminescence; if the excited carriers are created by high-energy electron bombardment of the material, the mechanism is called cathodoluminescence; if the excitation occurs by introduction of current in to the sample, the resulting luminescence is called electroluminescence. Other types of excitation are possible, but these three are the most important for device applications.

Nitride-based device structures for electronic and optoelectronic applications usually incorporate layers of $Al_xGa_{1-x}N$, and *n-* and *p*-type doping of these alloys is typically required. Challenges involved in doping of AlGaN films are briefly reviewed by Khan *et al*. [8]. As the bandgap of AlGaN increases with its Al composition, the ionization energies for silicon (n-type dopant) and magnesium (p-type dopant) increase too, resulting in a lower ionization efficiency. Therefore both n-type and p-type doping of AlGaN films is much more difficult than GaN. Sapphire substrates are electrically insulating, requiring fabrication of laterally conducting LEDs with both contacts on the

same side of the wafer. Higher resistivity of the n-contact AlGaN layer results in non-uniform current injection in the diode active area, known as 'current crowding'. Current crowding leads to increased injection currents along the perimeter of the LED mesa [11] [12].
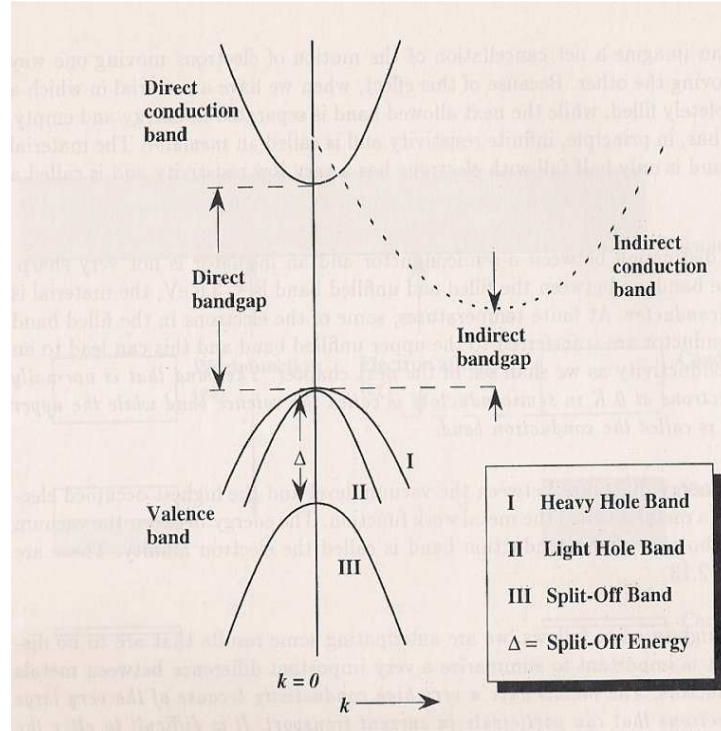
Figure 3.1: Schematic of the valence band direct bandgap and indirect bandgap conduction band

The ionization energy for Mg dopants in p-type GaN is already relatively high at 250 meV and it increases for AlGaN such that it is difficult to achieve conduction in p-type AlGaN with an Al composition greater than about 25–30%. It is also very difficult to make ohmic contacts to p-AlGaN films. [13] [14] Therefore, a thin p-GaN film is deposited on the top surface to serve as a contact layer, with this film absorbing some of the UV emission. Even if holes can be effectively injected from the metal into the p-GaN material, such holes are then faced with a potential barrier before they can be transported across subsequent AlGaN barrier layers down to the QWs. Holes that are trapped at the

29

first interface set up an electric field, which can attract electrons to avoid the QWs and hence recombine non-radiative in the p-GaN layer, and this has a major impact on the quantum efficiency.

The schematic of the valence band direct bandgap and indirect bandgap conduction band is shown in Figure 3.1 [16]. The bottom of the conduction band occurs at k=0 for direct bandgap semiconductors. GaAs, InP, InGaAs, AlN, GaN and InN are all direct bandgap semiconductor; the bandgap energy for AlN is 6.2 eV, for GaN it is 3.4 eV and for InN it is 0.6. Unlike the III-phosphide semiconductor materials the III-nitride system enables LEDs that emit green, blue, violet and even ultraviolet wavelengths. Near the top of the valence band, there are three important curves as shown in Figure 1, the heavier mass band is called the *heavy hole band*, the second lighter band is called *light hole band*, and the third band separated by an energy Δ, is called *the split-off band.* The masses of the valence band electrons are usually much heavier than those in the conduction band and are also negative.

3.1   P- AND N-TYPE SEMICONDUCTORS

As reviewed in previous chapters, we can see that one of the important factors affecting the LED efficiency is injection efficiency. The injection efficiency depends on an effective injection of electrons and holes into an active layer for radiative recombination. Electrons and holes in cladding layers of the active layer are generated by an intentional addition of impurities. The process of introducing dopant atoms into a lattice of a host semiconductor is called doping. The doping is classified into two basic types; negative (electrons) and positive (holes) type, depending on the type of dopants to produce free carriers in the semiconductor. The dopant atoms that give or donate an

electron are called donors and called acceptors for creating a hole. After the dopants accommodate in the semiconductor, they will form energy states within the bandgap of the semiconductor as a donor state and an acceptor state.

$$N_d \rightarrow N_d^+ + e \qquad \dots\dots\dots\dots\dots 3.1$$

When a donor state is ionized by donating an electron, it will be positive and it is neutral when occupied. In the other case, an ionized acceptor state is negative by accepting an electron and it will be neutral when empty.

$$N_a \rightarrow N_a^- + h \qquad \dots\dots\dots\dots\dots 3.2$$
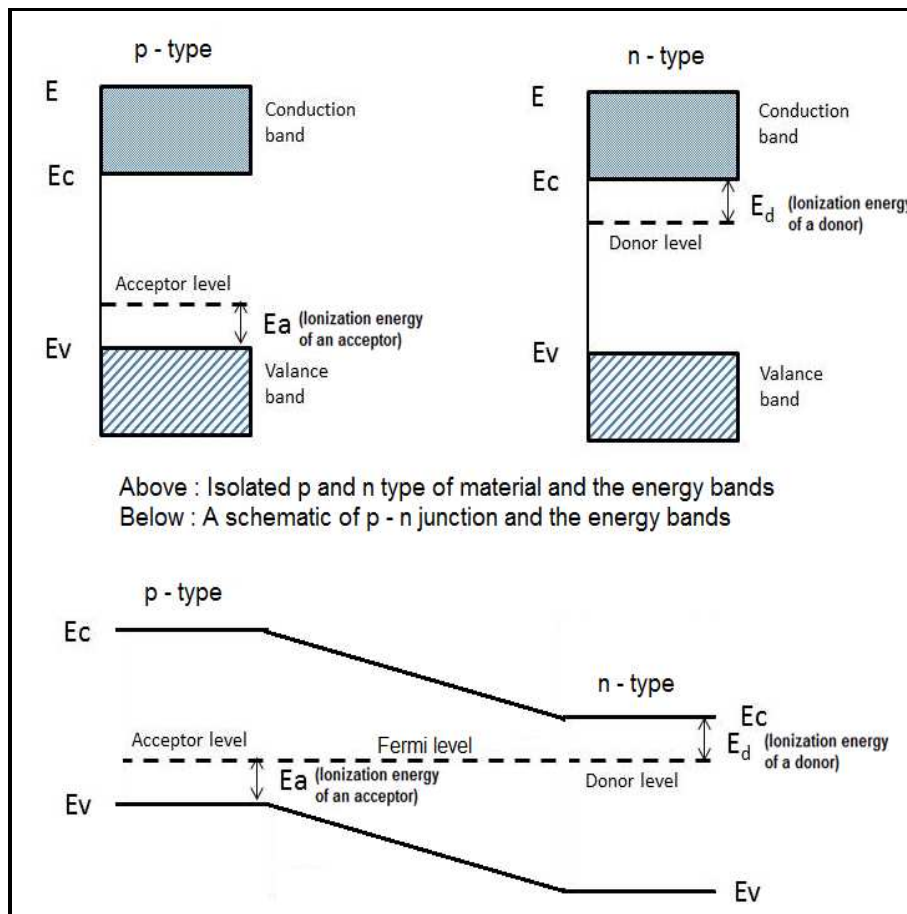
Figure 3.2: Energy bands for p - and n- type semiconductors

Mostly the ionization energy or activation energy of dopant states is analyzed by use of the simplest calculation based on the hydrogen-atom model. Using this model the electron mass is simply the effective mass at the bandage. This approximation is called the effective mass approximation for impurities. The ionization energy of a hydrogen atom is 13.6 eV, and can be determined using a following equation:

$$E_n^H = \frac{m_o\,e^4}{2(4\,\pi\varepsilon_o\,\hbar)^2\,n^2} \qquad \dots\dots\dots\dots\dots 3.3$$

The ionization energy of the donor ($E_d = E_C - E_D$) in a semiconductor lattice can be obtained by replacing m_o – free electron mass by the conductivity effective mass of electrons of m_{ce} and replacing ε_o by the permittivity of the semiconductor by ε_s. So, the ionization energy of the donor is given by the following equation:

$$E_d = \left(\frac{\varepsilon_o}{\varepsilon_s}\right)^2 \frac{m_{ce}}{m_o}\,E_H \qquad \dots\dots\dots\dots\dots 3.4$$

The acceptor ionization energy, ($E_a = E_A - E_V$), can also be calculated by using the conductivity effective mass of holes.

So far, n- type and p-type group III nitrides are accomplished commonly by Si and Mg doping. Their donor and acceptor activation energies in GaN are reported about 8-28 meV [16] and 150-250 meV [13], respectively and the donor and acceptor activation energies in AlN of 86 or 250-320 meV and the acceptor activation energies of 510 , 630 and 465 to 758 meV have been reported, respectively [16] [13]. These values show that the ionization energies of acceptors in both GaN and AlN are much larger than those of donors. Also shows that the ionization energies of donors and acceptors in GaN are smaller than in AlN explaining that donors and acceptors in GaN

are activated much more effective than in AlN. Although AlN is naturally insulating, making it a difficult material to dope n- or p-type, n- type AlN doped with Si can have electron concentration ~ 10^{15} to 7.4×10^{17} cm $^{-3}$, and p-type AlN with Mg-doping can have hole concentration ~ 10^{10} cm $^{-3}$ [17].

For Si- and Mg-doping in $Al_xGa_{1-x}N$, both ionization energies of Si and Mg increase with a higher Al content from 8 to 86 meV for Si in $Al_xGa_{1-x}N$ with $0 \leq x \leq 1$ and from 150 to 320 meV for Mg in $Al_xGa_{1-x}N$ with $0 \leq x \leq 0.7$ as presented in Figure 3.4 and Figure 3.3 [17] [14].
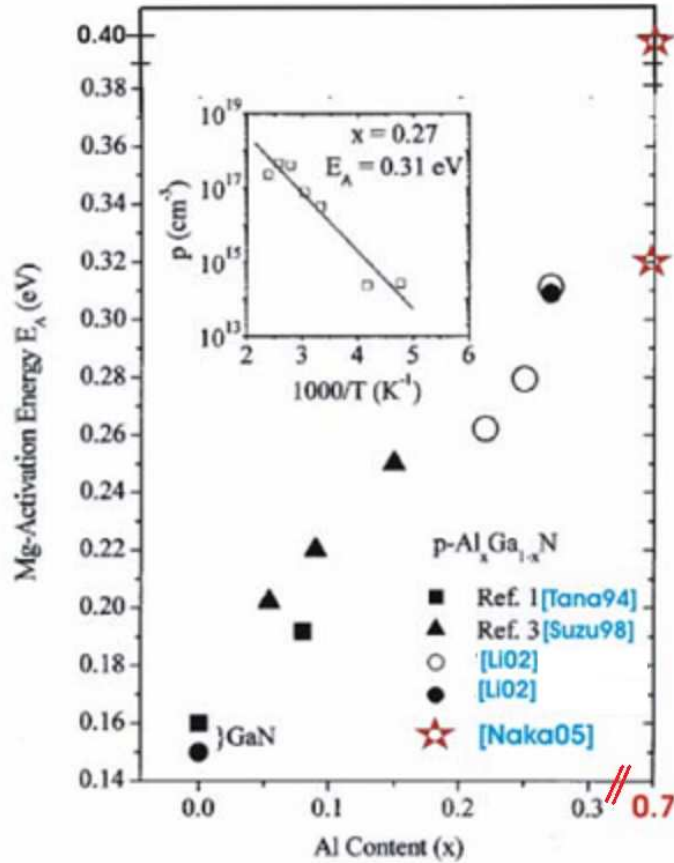
Figure 3.3: Activation energy of Mg acceptors in Mg-doped p-type $Al_xGa_{1-x}N$ as a function of Al content x.

33
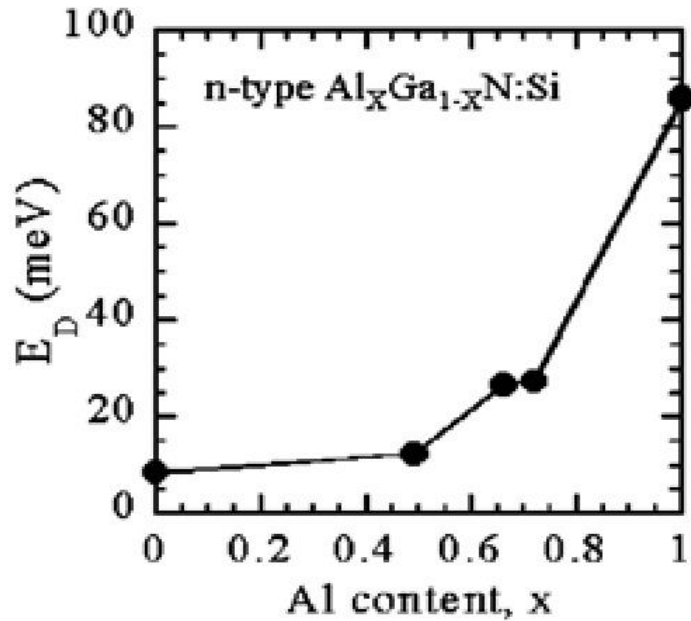
Figure 3.4: Ionization energies of Si in $Al_xGa_{1-x}N$

3.2   DOPING EFFICIENCY OF $AL_xGA_{1-x}N$

As known well, it is not difficult to achieve n-type group III nitrides due to unintentional impurity acting as donors in undoped layers. However, it is more difficult to obtain high n-type conductivity in $Al_xGa_{1-x}N$ layers with a high Al composition up to AlN layers respecting to larger activation energy. The bandgap of GaN = 3.42 eV and of AlN = 6.2 eV, with increasing Al composition the bandgap of $Al_xGa_{1-x}N$ increases depending on x value from as low as 3.42 eV (Al 0%) to 6.2eV (Al 100%), the ionization energies for silicon and magnesium increase too, resulting in a lower ionization efficiency. Therefore both n-type and p-type doping of AlGaN films is much more difficult than GaN.

For undoped semiconductor,

$$n = p = n_i \qquad \dots\dots\dots\dots\dots 3.5$$

and

34

$$E_F = E_i \qquad \ldots \ldots \ldots \ldots \ldots 3.6$$

This, leads to the following equations for n and p:

Total free electrons in conduction band,

$$n = n_i \, e^{\left(\frac{Ef - Ei}{kBT}\right)} \qquad \ldots \ldots \ldots \ldots \ldots 3.7$$

Similarly, total free holes in valence band,

$$p = n_i \, e^{\left(\frac{Ei - Ef}{kBT}\right)} \qquad \ldots \ldots \ldots \ldots \ldots 3.8$$

Because of the doping electrons and holes are not equal anymore, i.e.

$$n - p = \Delta n \neq 0 \qquad \ldots \ldots \ldots \ldots \ldots 3.9$$

For a semiconductor in a thermal equilibrium,

$$n.p = n_i^2 = N_c \, N_v \, \exp\left(\frac{-Eg}{kBT}\right) \qquad \ldots \ldots \ldots \ldots \ldots 3.10$$

At finite temperature, the electrons will be redistributed, but their numbers will be conserved and will satisfy the following equality resulting from charge neutrality:

This gives,

$$N_d^{+} - N_a^{-} + p - n = 0 \qquad \ldots \ldots \ldots \ldots \ldots 3.11$$

where, n = total free electrons in conduction band, n_d ($=N_d^{+}$) = number of electrons bound to the donors, p = total free holes in valence band and p_a ($= N_a^{-}$) = number of holes bound to the acceptors.

In order to find out what fractions of the donor (acceptor) atoms are ionized one need to know the distribution function for the impurity atoms. We can use a similar approach like Fermi-Dirac statistics function to calculate the probability function for

donor level which has an energy E_d measured from the conduction bandage. The ratio of ionized donor atoms to total available donor atoms is given by the following equation:

$$\frac{n}{Nd} = \frac{1}{\frac{N_c}{2N_d}exp\left(-\frac{(Ec-Ed)}{k_BT}\right)+1}$$ 3.12

where, E_d-E_c can be found using following equation

$$E_d = E_c - 13.6 \text{ eV } \left(\left(\frac{\varepsilon_o}{\varepsilon_s}\right)^2 \frac{m_e^*}{m_o}\right)$$ 3.13

Table 3.1: Electron effective masses of various Al content AlGaN

AlGaN composition	Effective electron masses m_e^* $[m_0]$ **	E_c-E_d [eV]
$Al_{0.0}$ GaN	0.186	0.0145
$Al_{0.25}Ga_{0.75}N$	0.223	0.0174
$Al_{0.50}Ga_{0.50}N$	0.267	0.0208
$Al_{0.75}Ga_{0.25}N$	0.268	0.0209
$AlGa_{0.0}N$	0.305	0.0238

*** J.R. Letite et al*

where, N_d = donor density, E_d = donor level energy measured from conduction band, Na = acceptor density, E_a = acceptor level energy measured from valence band, E_f = Fermi level energy, k_BT/e = 0.026 V. The plot of the carrier concentration versus temperature is shown in Figure 3.5. The plot was constructed assuming a phosphorous – doped N_D = 10^{15} /cm^3 Si sample n_i/N_D versus T (dashed line) has been included for comparison purpose.
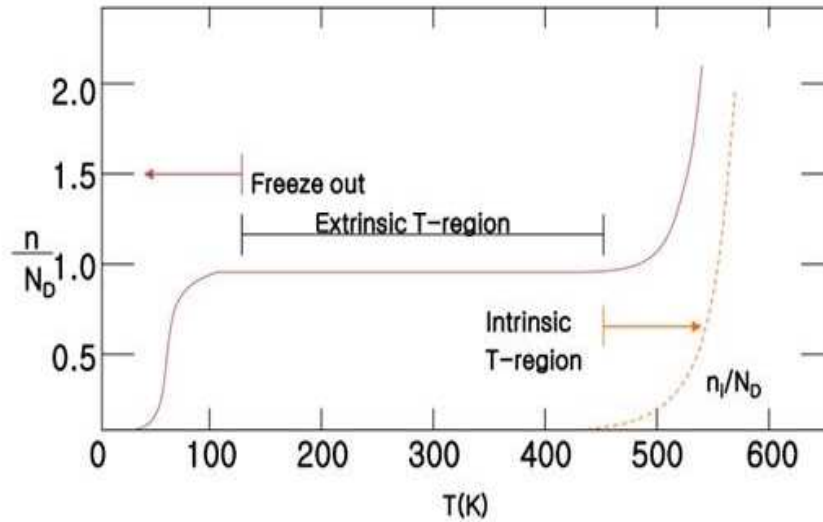
Figure 3.5: Typical temperature dependence of the majority – carrier concentration in a doped semiconductor.
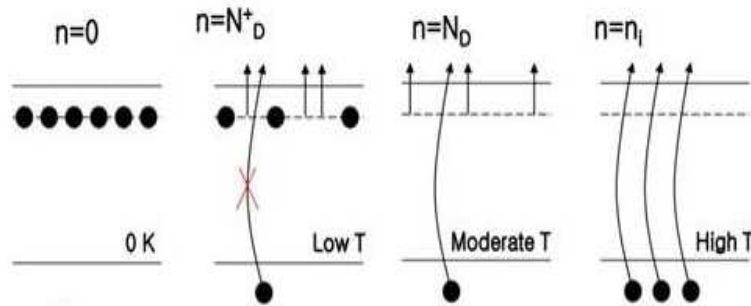
Figure 3.6: Qualitative explanation of the concentration – versus – temperature dependence displayed in Figure 3.5

There are three regions as shown in the above Figure 3.5, Freeze out, Extrinsic and Intrinsic regions and the carrier concentration and Fermi energy level can be derived for each region. At a very low temperature (freeze out region) close to zero Kelvin, all the donor atoms retain their electrons which do not have enough energy to be excited to the conduction band. All the states in the valence band are occupied by electrons which do not have enough energy to be excited across the relatively large bandgap. At slightly

higher but still low temperature the donor atoms will start to be excited to the conduction band according to the equation 3.12 and 3.13.

From Figure 3.3: Activation energy of Mg acceptors in Mg-doped p-type $Al_xGa_{1-x}N$ as a function of Al content x. Figure 3.3 and Figure 3.4 we can see that the activation energy of Si (n-type dopant) is much lower than activation energy for Mg (p type dopant) for similar x value in $Al_xGa_{1-x}N$. This will consequently results in a lower doping efficiency of Mg as compared to Si doping. From doping efficiency equations 3.12 and 3.13 we can see that as activation energy increases doping efficiency decreases. As discussed earlier in this chapter it is also consistent that with increase in the x value of $Al_xGa_{1-x}N$, the material bandgap increases and activation energy increases thus increase in x-value adversely affect the doping efficiency. In addition to ionization energy, the solubility limit of substitutional dopants in the host semiconductor also governs the achievable range of carrier concentration by intentional doping. With higher physical size and chemical similarity between the dopants and the host atoms, the solubility will be higher and it will be easier for the dopants to replace the host atoms.

3.3　GROWTH OF ALGaN SAMPLES AND CHARACTERIZATION

For doping study, first templates were grown on a c-plane sapphire using MOCVD system. The optimized nucleation layer thickness was adopted from the previous experiment described in Chapter 2. It is well established that insertion of SLs between high-quality AlN and n-AlGaN avoids cracking by modifying the strain properties of the epilayer structure and thus significantly improves the electrical properties of n-AlGaN [8] [19]. These research groups have also shown results which concludes that SL may play a crucial role in a pronounced reduction of screw-type

dislocations and/or other defects (such as point defects) and thus significantly improve overall quality of n-cladding AlGaN layers. To grow crack-free AlGaN layer with 1 µm thickness compositionally graded transition layers, superlattices were employed.

For three different AlGaN compositions three types of templates were used as shown in Figure 3.7. The samples were characterized for composition using optical transmission and 2theta scans from X-ray diffraction.
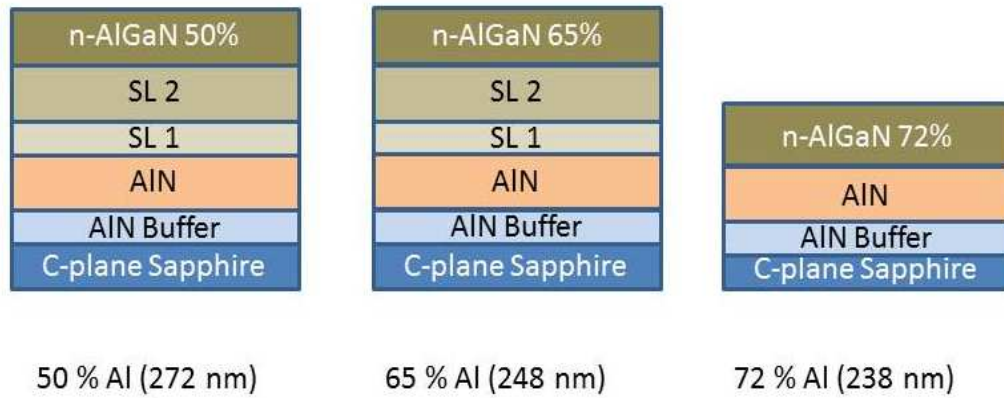
Figure 3.7: Epilayer structures for three different AlGaN compositions

The growth pressure was 50 Torr and temperature was 1000°C -1100 °C. Trimethylaluminium (TMA), trimethylgallium (TMG), and NH3 were used as precursors. 10 ppm SiH4 was used as the n-type dopant.

AlGaN compositions have been determined using 2 Theta Omega scans from X-ray diffraction. X-ray 2Theta scans for three types of $Al_xGa_{1-x}N$ compositions, x = 50, 65, and 72 % is shown in a combined graph as Figure 3.8. The structure of sample E, x = 50% and sample K, x = 65% have two sets of superlattice between AlN and AlGaN for strain compensating mechanism and crack-free thin-films. Superlattice one and two peaks can be seen between AlN peak and AlGaN zero peaks.

39

3.3.1 X-ray diffraction

X-ray diffraction (XRD) is a widely-used technique in materials science, as a highly sensitive tool for detailed structural studies.

X-ray diffraction can be explained in simple terms by the "reflection" of an incident X-ray beam from a stack of parallel equidistant atomic planes. The electrons that surround the atoms, rather than the atomic nuclei themselves, are the entities which physically interact with the incoming X-ray photons. At each atomic plane a small portion of the beam is reflected. If those reflected beams do not cancel each other by interference, a diffracted beam can be observed. The condition where the reflected beams interfere positively (add up in phase) to give a strong diffracted beam is given by Bragg's law. The Bragg law may be written as:

$$n\lambda = 2d_{hkl}sin\theta \qquad \ldots \ldots \ldots \ldots \ldots 3.14$$

Where, *n* is an integral number describing the order of reflection, λ is the wavelength of the X-rays, d_{hkl} is the spacing between the lattice planes and θ is the Bragg angle where a maximum in the diffracted intensity occurs. At other angles there is little or no diffracted intensity, because of negative interference. Since we know λ and we can measure θ, we can calculate the interplanar spacings. The characteristic set of d_{hkl} spacings generated in a typical X-ray scan provides a unique "fingerprint" of the material. Using adequate incidence angles, various information about the crystal structure, composition or imperfections can be obtained. Philips Panayltical X'Pert Pro MRD system was used in this work.
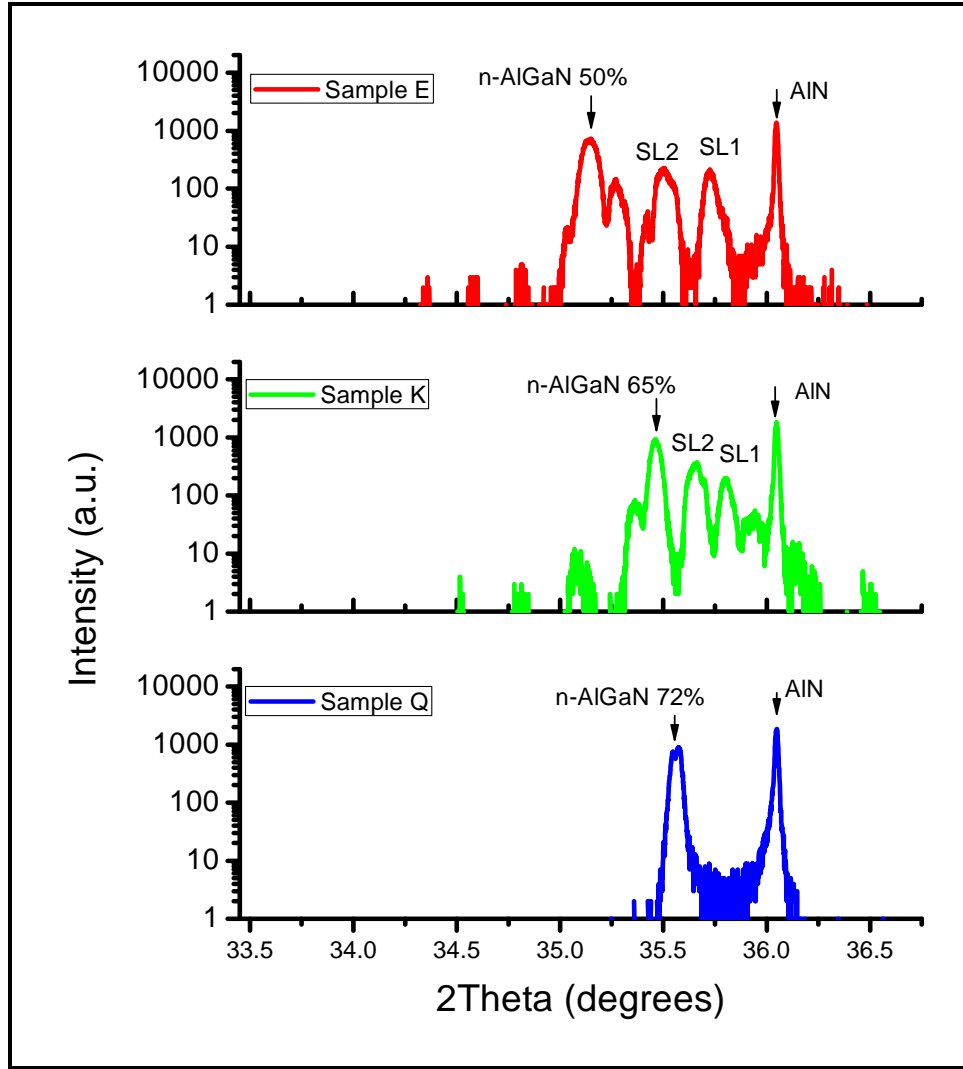
Figure 3.8: X-ray Diffraction 2Theta scan of $Al_xGa_{1-x}N$, x = 50 %, 65% and 72%

Table 3.2: x-value of $Al_xGa_{1-x}N$, from X-ray 2Theta angle

Sample	2Theta [degree]	d [angstrom]	x-value %
e	35.25	5.0861	48.71
k	35.45	5.0583	62.4
q	35.58	5.0404	71.2

Table 3.2 shows the x-values calculated from 2Theta angle of X-ray diffraction of each sample type using the Vegard's law: c(AlGaN) = c(AlN)x + c(GaN)(1-x).

3.3.2 Optical Transmission of Samples

The thickness measurement of the samples was done using optical transmission spectrum and equation shown here. The composition of the AlGaN was also calculated using Vegards' Law.
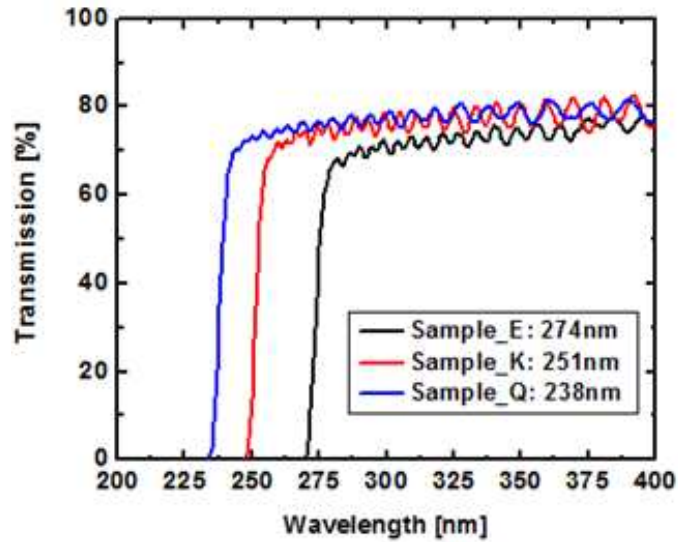
Figure 3.9: Optical transmission spectrum of various AlGaN compositions

$$d = \frac{1}{4n} x \frac{1}{(\frac{1}{\lambda_2} - \frac{1}{\lambda_1})} \qquad \ldots \ldots \ldots \ldots \ldots 3.15$$

Where d is film thickness, n is refractive index of layer, λ_1 is wavelength maxima, and λ_2 is wavelength minima.

Figure 3.10: Al content and wavelength chart using Vegards' Law

42

3.3.3 Atomic Force Microscopy

Atomic force microscopy (AFM) provides three-dimensional surface topography at nanometer lateral and sub-angstrom vertical resolution on semiconductors and other materials. A sharp tip 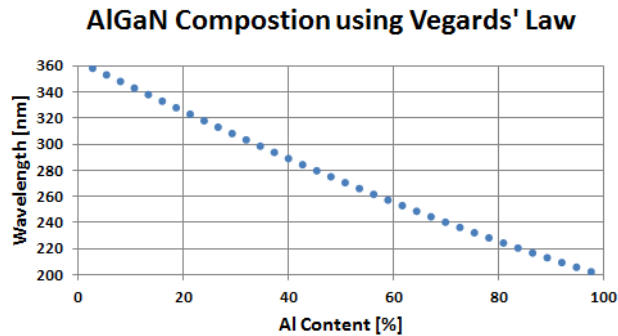on the end of a flexible cantilever scans a sample surface, while maintaining a constant force. The surface is scanned by a piezoelectric tube that moves the tip in a raster pattern with respect to the sample. The tip-sample interaction is monitored by reflecting a laser off the back of the cantilever into a split photodiode detector. By detecting the difference in the photodetector output voltages, changes in the cantilever deflection or oscillation amplitude are determined.

The two most commonly used modes of operation are contact mode and tapping mode. In this work the samples were investigated using the tapping mode. Here the cantilever is oscillating close to its resonance frequency (typically $\gg$ 300 kHz) and lightly tapping on the surface during the scan. The laser deflection method is used to detect the root-mean-square (rms) amplitude of the cantilever oscillation. A feedback loop maintains a constant oscillation amplitude by moving the scanner vertically at every x,y data point. Recording this movement forms the topographical image.

For investigation of atomically smooth surfaces, the AFM is very suitable, since the AFM possesses a very good vertical resolution. It can resolve monoatomic steps on the sample surface as well as calculate an rms roughness of the surface. Surface morphology investigations for the grown AlN and AlGaN layers were performed by Dimension Edge atomic force microscopy (AFM) operating in tapping mode. The rms roughness of the surface was calculated using the AFM software.
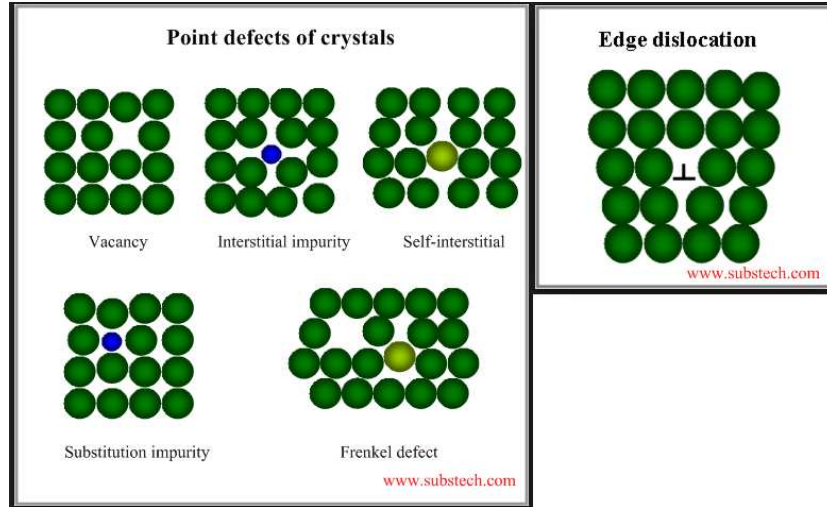
Figure 3.11: Types of defects in epitaxial layers

From Figure 3.12, we can see that with 50 % x-value of $Al_xGa_{1-x}N$ and increasing silane doping the surface morphology deteriorates. This is due to increase in point defects and increased edge dislocation.
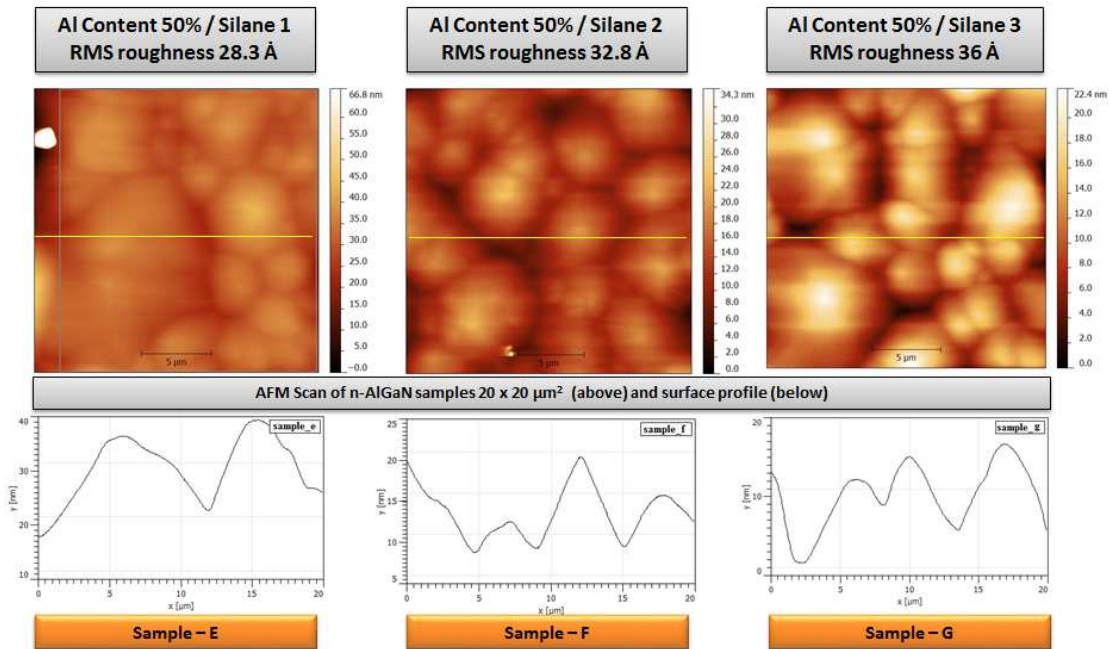

Figure 3.12 AFM scans and surface profile of 50% AlGaN
with change in silane for all three samples

3.3.4 Electronic Characterization of samples

Electronic characterization of materials evolved in three levels of understanding. In the early 1800s, the resistance R and conductance G were treated as measurable physical quantities obtainable from two-terminal current (I) – Voltage (V) measurements .The resistance alone was not comprehensive enough since different sample shapes gave different resistance values. This led to the understanding of a second level characterization of a material. The focus turned to an intrinsic material property like resistivity or conductivity, which is not influenced by the particular geometry of the sample. For the first time, this allowed scientists to quantify the current-carrying capability of the material and carry out meaningful comparisons between different materials. By the early 1900s, it was realized that resistivity was not a fundamental material parameter, since different materials can have the same resistivity. Also, a given material might exhibit different values of resistivity, depending upon how it was synthesized. This is especially true for semiconductors, where resistivity alone could not explain all observations. Theories of electrical conduction were constructed with varying degrees of success, but until the advent of quantum mechanics, no generally acceptable solution to the problem of electrical transport was developed. The third level of understanding includes the definitions of carrier density (n) and mobility (μ) which are capable of dealing with even the most complex electrical measurements today.

For this study doping of the AlGaN samples have been characterized using Hall measurement, Transmission line measurement and sheet resistance mapping.

3.3.5 Sheet resistance mapping

Setup for sheet resistance mapping is shown in the following Figure 3.13. LEI 1510 is a quick and noninvasive measurement technique. The LEI custom software generates the graphical image of scanned points in less than two minutes to scan through the entire wafer. Since this technique does not involve any physical contact with epitaxial layers and contact quality is irrelevant. The sample scan is shown in the Figure 3.14.

Figure 3.13: Sheet resistance maping setup LEI 1510
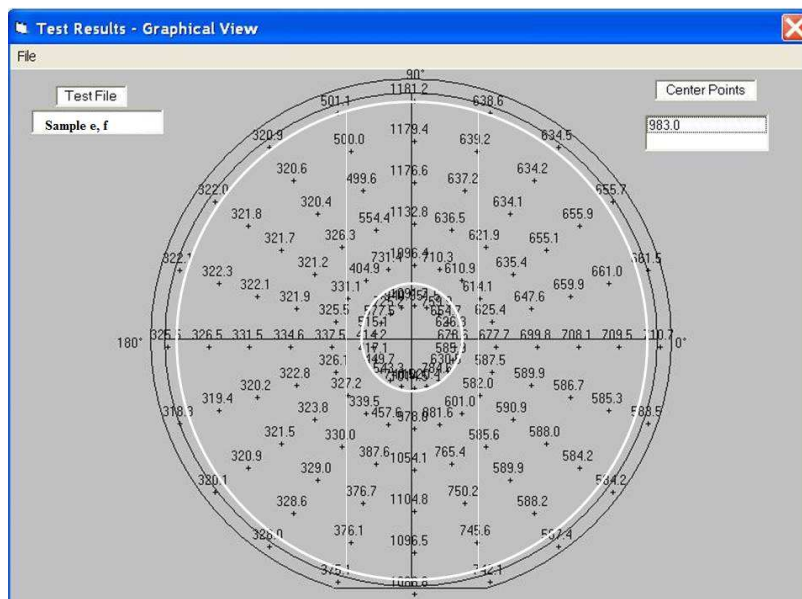
Figure 3.14: Sheet resistance of n-AlGaN sample shown graphically

3.3.6 Transmission Line Measurement (TLM)

Transmission Line Measurement have been used to determine the contact resistance between metal and semiconductor as well as sheet resistance of the semiconductor layer. For TLM measurements ohmic contacts c_1 to c_5 were deposited as shown in the Figure 3.15: TLM measurement. The length L and width Z and spacing between contact pads are shown in the Table 3.3. The area between contact pad is the isolation mesa of the semiconductor layer. Current I, and voltage V were measured to determine the resistance between tow metal pads. The graph of contact separation versus resistance for sample -e is shown in Figure 3.16. TLM results for all other samples are included in final results as shown in the Table 3.3.
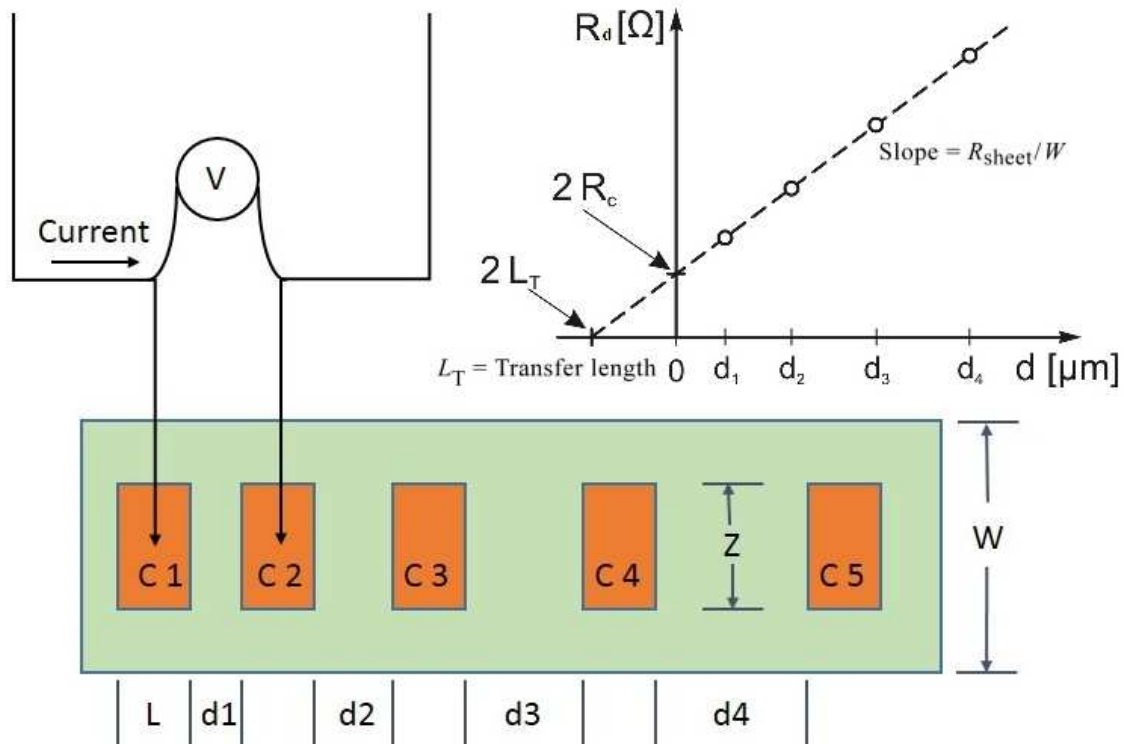
Figure 3.15: TLM measurement

Table 3.3: TLM measurements of Sample - e

Sample- e	Contact separation [μm]	Rd [Ω]	Vb @ 20mA
1	4.00	27.42	0.03870
2	6.00	31.84	0.03754
3	8.00	39.84	0.03388
4	10.00	40.47	0.03517
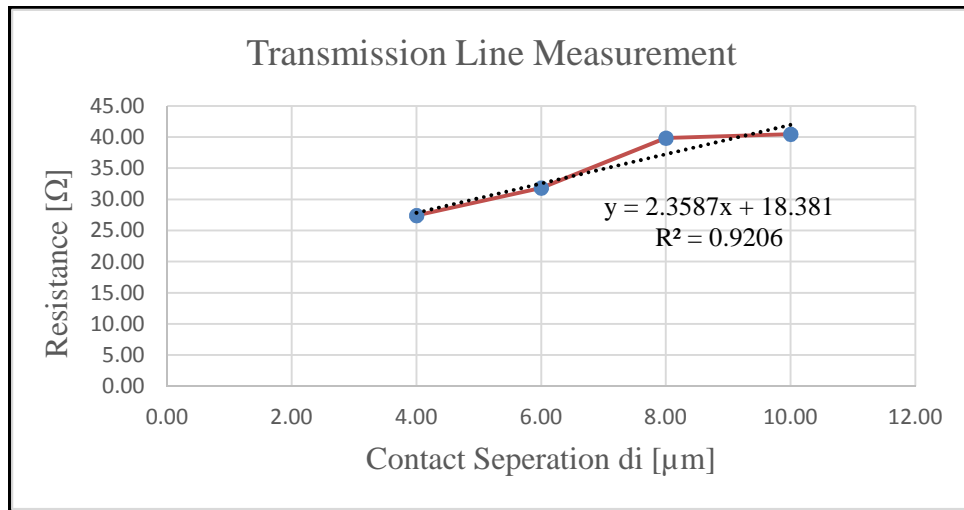
Figure 3.16: Resistance versus Contact separation from TLM

Table 3.4: Results from TLM measurement for sample - e

R_0	Ω		18.38
Z	μm		200
Sheet resistance Rsh	Ω/□	slope x Z	471.7
Transfer Resistance	Ω-mm	R_0 x Z	3.676
Specific contact Resistance Rc	Ω- cm^2		7.16E-05

3.3.7 Hall measurement

The key feature of hall measurements is the ability to determine the carrier density, the carrier type, and the mobility with a relatively simple method.
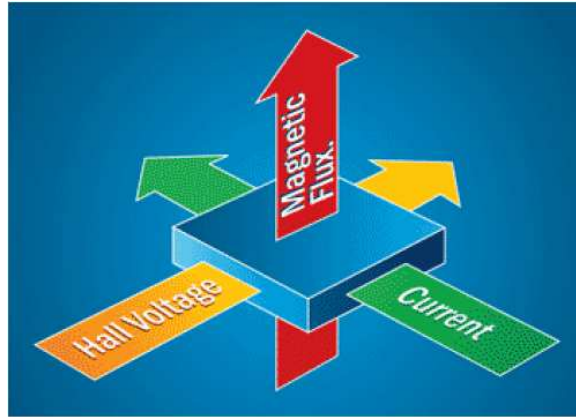
Figure 3.17: The Hall Effect and the Lorentz Force

The basic physical principle underlying the Hall effect is the Lorentz force, which is a combination of two separate forces: the electric force and the magnetic force. When an electron moves along the electric field direction perpendicular to an applied magnetic field, it experiences a magnetic force $-qv \times B$ acting normal to both directions.

Figure 3.18: Hall and Van der Pauw setup

3.4 RESULTS AND DISCUSSION

Table 3.5: Comprehensive results from various characterizations

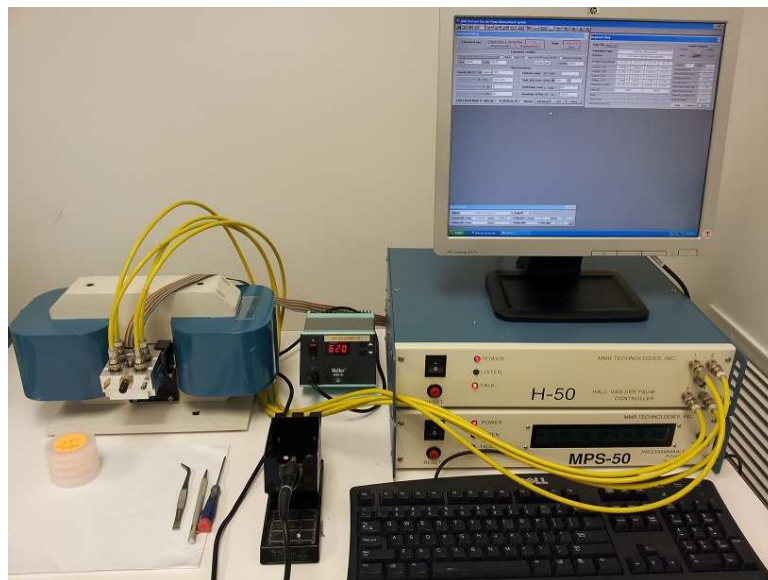| Samples	Sample Optical Cutoff [nm]	n-AlGaN Thickness [µm]	Silane Input **	AlGaN FWHM [arcsec]	RMS Roughness [Å]	Rsh average [Ω/□]	Rsh min [Ω/□]	Standard Deviation [%]	Available Carriers [cm⁻³]	RSh (Ohm/cm²)	Mobility (cm²/Vs)	Carrier Density (cm⁻³)	Carrier Type	Rsh [Ω/□]	Doping Efficiency [%]	AlGaN Comp. [Al %]
E	274	1.10	1	97	28.2	609	586	n/a	2.39E+19	337	24	7.65E+18	electrons	472	32	50%
F	275	1.14	2	103	32.8	342	335	n/a	4.77E+19	207	37	8.06E+18		225	17	
G	273	1.04	3	78	36	241	238	n/a	7.16E+19	127	21	2.37E+19		169	33	
H	273	1.15	4	178	34	186	181	n/a	9.55E+19	102	22	2.80E+19		138	29	
I	271	1.07	6	91	32	125	124	n/a	1.43E+20	84	33	2.25E+19		127	16	
K	251	0.84	1	59	32	752	712	n/a	2.39E+19	884	28	2.50E+18	electrons	853	10	65%
L	248	0.78	2	48	28	486	471	n/a	4.77E+19	401	25	6.13E+18		391	13	
M	249	0.90	3	53	35	353	345	n/a	7.16E+19	236	25	1.06E+19		370	15	
O	248	0.80	4	75	35	271	268	n/a	9.55E+19	251	34	7.32E+18		527	8	
U	238	0.96	1	59	23	884	818	5.4	2.39E+19	958	34	2.98E+18	electrons	n/a	12	72%
V	238	0.98	2	72	36	568	489	9	4.77E+19	580	47	2.31E+18		n/a	13	
W	239	0.99	3	55	30	771	391	37	7.16E+19	350	19	9.31E+18		n/a	5	
X	238	0.98	4	61	31	569	290	41	9.55E+19	397	37	4.25E+18		n/a	4	
** proprietary information removed for silane, simply standard flow rate multiplier is used																

From comprehensive characterization results shown in Table 3.5, doping efficiency on $Al_xGa_{1-x}N$, for x = 50, has been found 32 % for silane = 1. For the similar silane doping efficiency reduced to 10 % for x = 65 %, and 12 % for x = 72%. With the higher silane doping = 4, the efficiencies have been found to be 29, 8 and 4 % for x-values 50, 65, and 72%. These results are consistent with doping efficiency equation 3.12 and we can conclude that doping efficiency for $Al_xGa_{1-x}N$ reduces with increase in x-value.
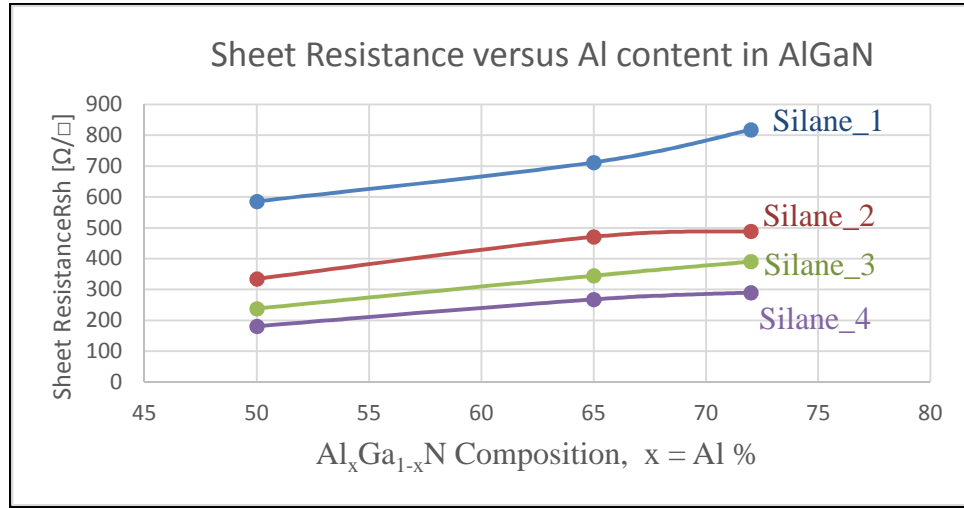

Figure 3.19: Sheet Resistance versus Al content in AlGaN

We can clearly see the similar trend in Figure 3.19, as x-value increases the sheet resistance increases even when the silane flow is same for various AlGaN composition. This is true for all samples having various silane doping. This results are also consistent with doping efficiency equation. As x-value increases, doping efficiency reduces and sheet resistance increases. Carrier density and doping efficiency versus Al content results are shown in the following charts Figure 3.20 and Figure 3.21. Carrier density significantly reduces with the increase in Al content.
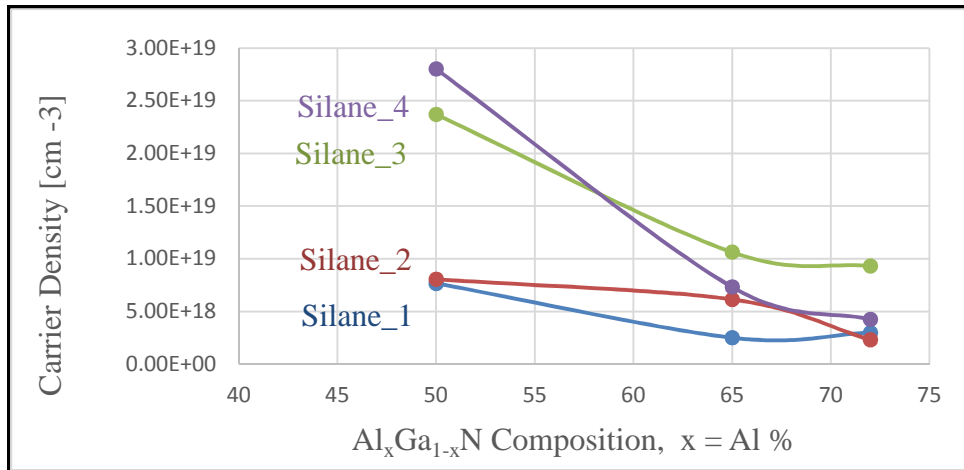
Figure 3.20: Carrier Density versus Al content in AlGaN
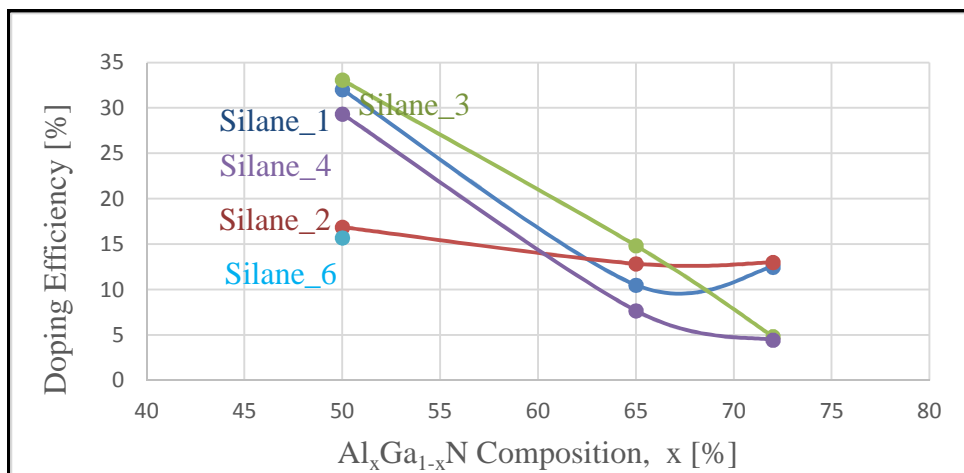
Figure 3.21: Doping Efficiency versus Al content in AlGaN alloy

Figure 3.22: Silane Flow versus Carrier Density

52

Sheet resistance results from two measurement techniques, sheet resistance mapping, and hall measurement are shown in Figure 3.23 and Figure 3.24. Both results are consistent with doping efficiency equation.

Figure 3.23: Sheet Resistance from Hall Measurement versus Silane Flow

Figure 3.24: Silane Flow versus Sheet Resistance measured using Rsh _Mapping

CHAPTER 4: CONCLUSIONS

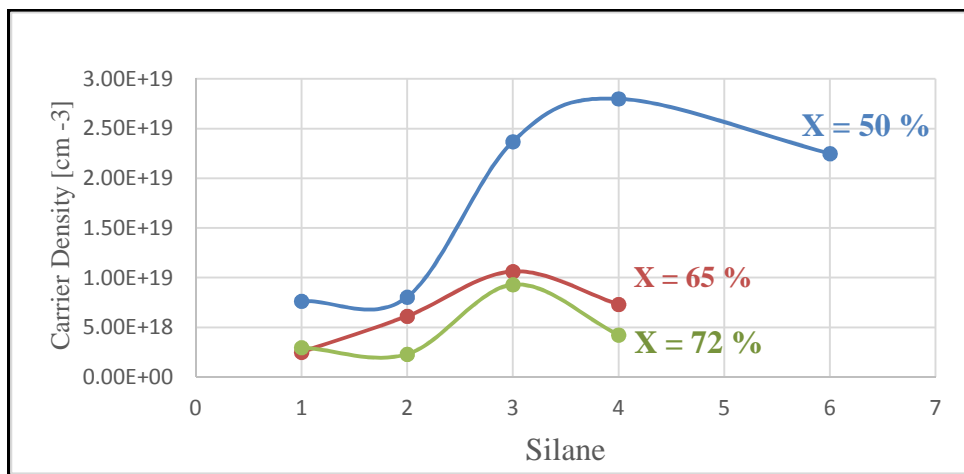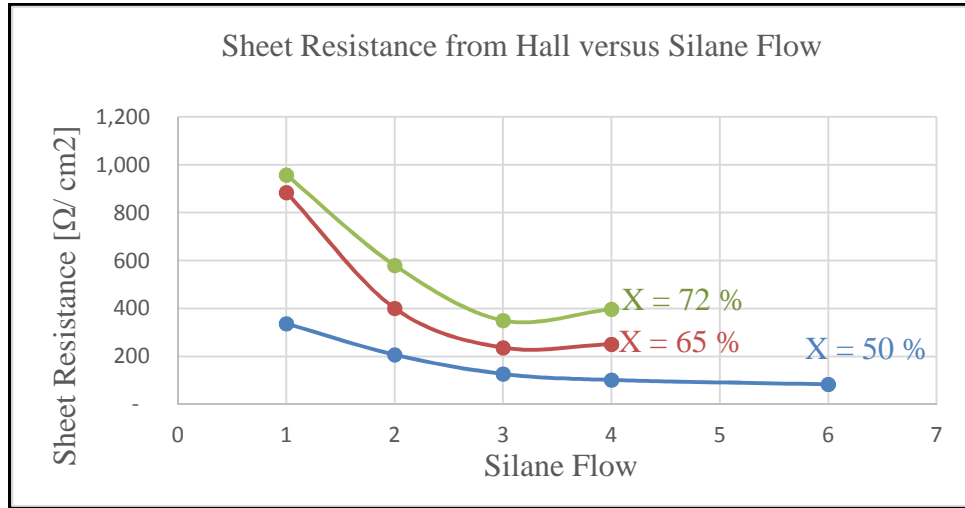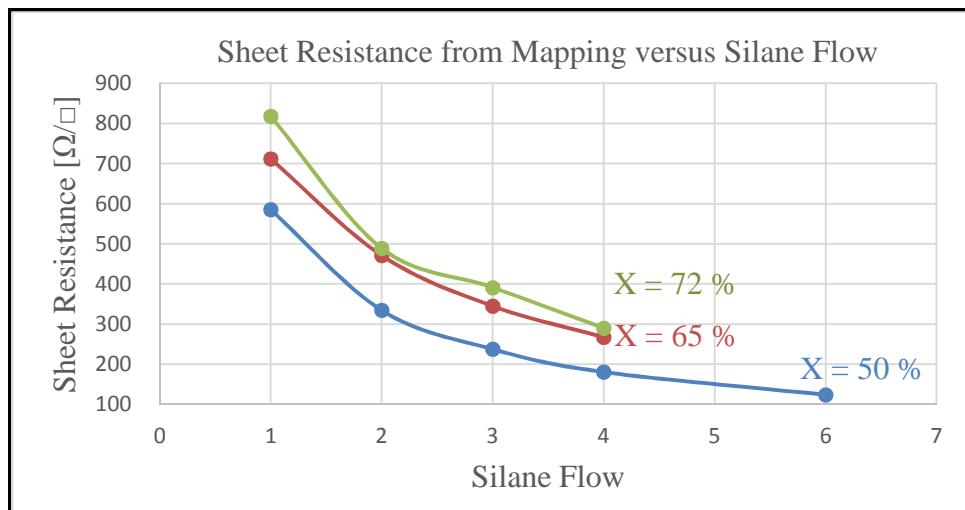The comprehensive results, and all relevant charts show that as the doping concentration increased, carrier concentration was found to monotonically increase whereas doping efficiency reduced. Carrier concentrations were found to reduce with increased Al concentration, as expected due to increased ionization energy. Calculated doping efficiency was found to be consistent with doping efficiency equation. However, optimization of AlGaN quality strongly seems depend on the nucleation layer thickness. It is a crucial act of balancing, thinner buffer layer leads to poor quality of epitaxial layer and thicker ends up being highly cracked, thus optimum buffer thickness may help us achieving higher yield and efficiency of devices. From comprehensive results we can also conclude that optimized doping concentration is a key to higher efficiency and higher yield for semiconductor devices.

Table 4.1: 121 Point Sheet Resistance Mapping of AlGaN with 72% Al content

Silane Input	Rsh - average	Rsh - min	Standard Deviation
**	$[\Omega/\square]$	$[\Omega/\square]$	[%]
1	884	818	5.4
2	568	489	9
3	771	391	37
4	569	290	41
** proprietary information removed for silane, simply standard flow rate multiplier is used			
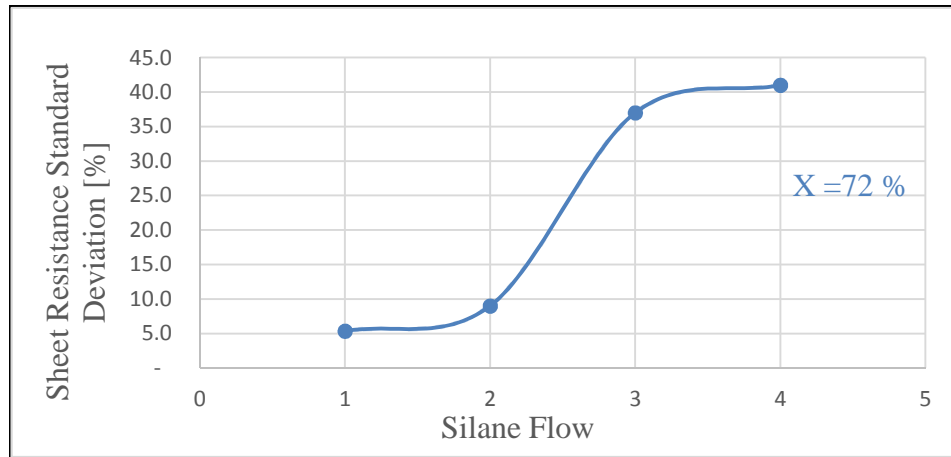
Figure 4.1 : Sheet Resistance Standard Deviation versus Silane flow over 2" wafer

We can summarize conclusions as per following:

- ✓ Increase in standard deviation of sheet resistance is indicative of material quality degradation.

- ✓ Overall doping efficiency and carrier density reduces for AlGaN with higher Al content.

- ✓ Sheet resistance increases for higher Al content AlGaN

- ✓ Increase in standard deviation of sheet resistance is indicative of material quality degradation.

- ✓ Sheet resistance reduces with increase in Si doping

- ✓ For similar Al content AlGaN, increase in silane doping increases the RMS roughness.

CHAPTER 5: FUTURE WORK

Impurity doping as name suggests will modify the undoped crystal structure to make it n- or p- type of semiconductor. However polarization doping is a non-traditional way to get doping. Polarized doping may be employed along with substitutional doping. Instead of single composition of n-type layer, super lattice type n-layer may be employed. Balanced doping, proportional to Al Content in superlattice type structures may help maintain better quality of material along with the required carrier concentration

REFERENCES

[1] Ambacher_O, "Growth and Applications of Group III-nitrides," *Journal of Physics,* vol. 31, pp. 2653-2710, 1998.

[2] S.C.Jain, M. Willander, J. Narayan and R. V. Overstraeten, *Journal of Applied Physics,* vol. 87, p. 965, 2000.

[3] "http://www.veeco.com/molecular-beam-epitaxy.aspx," Veeco, 1 June 2013. [Online]. Available: http://www.veeco.com. [Accessed 1 June 2013].

[4] "http://www.gslb.cleanrooms.com/online-articles/2011/2.Par.36289.Image.620.341.1.gif," 2011. [Online]. Available: http://www.gslb.cleanrooms.com. [Accessed 17 May 2013].

[5] H. Hirayama, "Developing the world's highest output in deep-UV light-emitting diode technology," 20 January 2012. [Online]. Available: http://www.rikenresearch.riken.jp/eng/frontline/6923. [Accessed 4 May 2013].

[6] P. Bhattacharaya, Semiconductor Optoelectronic Devices, New Jersey: Prentice Hall, 1993.

[7] "LED Color Mixing: Basics and Background," *CREE,* 2013.

[8] M. Shatalov, Z. Gong, M. Gaevaski and M. A. Khan, "Reliability of AlGaN - based deep UV LEDs on sapphire," in *Proc. of SPIE Vol 6134 61340P-1*, 2006.

[9] X. Wang, D. Zhao, X. Li, H. Gong, H. Yang and J. Liang, "The effects of LT AlN buffer thickness on the properties of high Al composition AlGaN epilayers," *Science Direct,* no. 60, pp. 3693-3696, 2006.

[10] X. Wang, D. Zhao, X. Li, H. Gong, H. Yang and J. Liang, "The effects of LT AlN buffer thickness on the optical properties of AlGaN grown by MOCVD and Al composition inhomogeneity analysis," *Journal of Physics D: Applied Physics,* no. 40, pp. 1113-1117, 2007.

[11] H. Amano and I. Akasaki, "Novel aspects of growth of nitrides by MOVPE," *Journal of Physics,* vol. 13, pp. 6935-6944, 2001.

[12] V. Adivarahan, A. Heidari, B. Zang, Q. Fareed, K. Balkrishnan and A. Khan, "Vertical Injection Thin Film Deep Ultraviolet Light Emitting Diodes with AlGaN multiple-Quantum Wells Active Region," *Applied Physics Express,* vol. 2, pp. 092-102, 2009.

[13] K. Forghani, L. Schade, U. T. Schwarz, F. Lipski and F. Scholz, "Strain and defects in Si-doped (Al)GaN epitaxial layers," *Journal of Applied Physics,* vol. 112, pp. 093-102, 2012.

[14] H. X. Jiang and J. Y. Lin, "AlGaN and InAlGaN alloys - epitaxial growth, optical and electrical properties and applications," *Opto - Electronics Review,* vol. 10, no. 4, pp. 271-286, 2002.

[15] N. Nepal, M. Nakarmi, J. Lin and H. Jiang, "Temperature and compositional dependence of the energy band gap of AlGaN alloys," *Applied Physics Letters,* vol. 87, 2005.

[16] J. Singh, Semiconductor Devices An Introduction, McGraw-Hill, Inc, 1994.

[17] Y. Taniyasu, M. Kasu and N. Kobayashi, "Intentional control of n-type cundduction for Si doped AlN and AlxGa1-xN for x .42 to 1," *Applied Physics Letter,* vol. 81, 2002.

[18] Y. Taniyasu, M. Kasu and T. Makimoto, "An Aluminium Nitride Light-Emitting Diode with a wavelength of 210 nanometers," *Nature,* vol. 441, 2006.

[19] C. Pernot, S. Fukahori, T. Inazu, I. Akasaki and H. Amano, "Development of High efficiency 255-355 nm AlGaN-based light-emitting diodes," *Phys. Status Solidi,* pp. A, 1-3, 2011.

[20] Q. S. Paduano, D. W. Weyburne and Z. L.-W. J. Jasinski, "Effect of initial process conditions on structural properties of AlN films," *Journal of Crystal Growth,* vol. 261, pp. 259-265, 2004.

[21] R. Dalmau, S. Craft, B. Moody, S. Mita and Z. Sitar, "Challenges in AlN Crystal Growth and Prospects of AlN-based Technology," in *CS MANTECH Conference*, Palm Spring, California, 2011.

[22] A. Armstrong, A. A. Allerman, T. A. Henry and M. H. Crawford, "Influence of Growth temperature of AlGaN multiquantum well defect incorporation and photoluminescence efficiency," *Applied Physics Letters,* vol. 98, 2011.

[23] A. Fujioka, T. Misaki, T. Murayama and T. Mukai, "Improvement in Output Power of 280-nm Deep Ultraviolet Light-Emitting Diode by Using AlGaN Multi Quantum Wells," *Applied Physics Express,* vol. 3, 2010.

[24] J. Piprek, "Ultra-violet light-emitting diodes with quasi acceptor-free AlGaN polarization doping," *Opt Quant Electron,* vol. 44, pp. 67-73, 2012.

[25] J. R. Grandusky, S. R. Gibb, M. C. Mendrick and L. J. Schowalter, "Properties of Mid-Ultraviolet Light Emitting Diodes Fabricated from Pseudomorphic Layers on Bulk Aluminum Nitride Substrates," *Applied Physics Express,* vol. 3, 2010.

[26] "Temperature Dependence of Silicon Doping of GaAs by SiH4 and Si3H6 in Atmospheric pressure MOCVD," *Elsevier Science Publisher B. V. ,* vol. 89, pp. 0022-0248, 1989.

[27] R. Paiva, J. Alves, R. Nogueira, C. Oliveira, L. Scolfaro and J. Leite, "Theoretical study of the AlxGa1-xN alloys," *Material Science and Engineering,* vol. B93, pp. 2-5, 2002.

[28] M. Cooke, "Going deep for UV sterilization LEDs," *Semiconductor Today,* pp. 82-88, April/May 2010.